Clumps as multiscale structures in cosmic noon galaxies

Boris S. Kalita [1,2,3]⋆† Tomoko L. Suzuki [1,3] Daichi Kashino,[4] John D. Silverman,[1,3,5,6]
Emanuele Daddi [7] Luis C. Ho,[2,8] Xuheng Ding,[9] Wilfried Mercier,[10] Andreas L. Faisst,[11]
Kartik Sheth,[12] Francesco Valentino [13,14] Annagrazia Puglisi [15] Toshiki Saito,[16] Darshan Kakkad [17]
Olivier Ilbert,[10] Ali Ahmad Khostovan [18,19] Zhaoxuan Liu,[1,3,20] Takumi Tanaka [1,3,20]
Georgios Magdis [13,14,21] Jorge A. Zavala,[4] Qinghua Tan,[22] Jeyhan S. Kartaltepe,[18] Lilan Yang [18]
Anton M. Koekemoer [23] Jed McKinney,[24] Brant E. Robertson,[25] Shuowen Jin [13,21]
Christopher C. Hayward [26] Michaela Hirschmann [27,28] Maximilien Franco,[24] Marko Shuntov,[13,14]
Ghassem Gozaliasl,[29,30] Aidan Kaminsky[31] and R. Michael Rich [32]

Affiliations are listed at the end of the paper

ABSTRACT

Star-forming clumps have been found to significantly influence the star formation of gas-rich $z > 1$ galaxies. Using public data from *JWST*/NIRCam (Cosmic Evolution Survey; COSMOS-Web) and Atacama Large (sub-)Millimeter Array (ALMA; Fiber-Multi Object Spectrograph or FMOS-COSMOS survey), we study a sample of 32 massive ($> 10^{10.5}\,M_\odot$) main-sequence galaxies at $z_{\rm spec} \sim 1.5$ with $\sim 0.3\,{\rm kpc}$ resolution. We create composite morphological models consisting of bulge, disc, and clumps to fully 'deconstruct' the galaxy images. With the resulting measurements of the flux and size of these components, we find the following: (i) the combined contribution of clumps is 1–30 per cent towards the net star formation of the host while contributing 1–20 per cent to its stellar mass. The clumps show a correlation between their stellar mass and star formation rate (SFR), but have an increased specific SFR relative to the star formation main-sequence, with offsets ranging from $0 \lesssim \Delta \log {\rm sSFR} \lesssim 0.4$. They feature star formation surface densities of $10^{-2} - 10^2\,M_\odot\,{\rm yr}^{-1}\,{\rm kpc}^{-2}$, consistent with values observed in both local star-forming and starburst galaxies. (ii) The detected clumps span a large range of characteristic sizes ($r_e \sim 0.1 - 1\,{\rm kpc}$) and stellar masses ($\sim 10^{8.0-9.5}\,M_\odot$). We estimate a mass–size relation ($r_e \propto M_\star^{0.52\pm0.07}$) along with a stellar mass function (slope, $\alpha = -1.85 \pm 0.19$), both suggesting a hierarchical nature similar to that expected in star-forming regions in local galaxies. (iii) Our measurements agree with the properties of stellar clumps in $z \gtrsim 1$ lensed systems, bridging the gap between lensed and unlensed studies by detecting structures at sub-kpc scales. (iv) Clumps are found to be preferentially located along spiral features visible primarily in the residual rest frame near-IR images. In conclusion, we present an observation-based, coherent picture of star-forming clumps in galaxies at $z > 1$.

Key words: galaxies: evolution – galaxies: structure.

1 INTRODUCTION

The highly clumpy nature of star-forming galaxies at $z > 1$ has been recognized for nearly three decades (Abraham et al. 1996; van den Bergh et al. 1996; Elmegreen & Elmegreen 2005; Elmegreen, Bournaud & Elmegreen 2008; Förster Schreiber et al. 2011; Wuyts et al. 2012; Guo et al. 2015; Shibuya et al. 2016; Soto et al. 2017; Guo et al. 2018; Huertas-Company et al. 2020). Due to their high gas fractions, these galaxies likely experience instabilities from fragmentation (Daddi et al. 2008, 2010; Tacconi et al. 2010, 2013; Geach et al. 2011; Magdis et al. 2012; Béthermin et al. 2015;

Claeyssens et al. 2023; Rujopakarn et al. 2023). Stellar clumps (which will be referred to as 'clumps' throughout this work) formed under such conditions are expected to be more massive than similar structures observed at lower redshifts (Cowie, Hu & Songaila 1995; Cook et al. 2016; Larson et al. 2020; Mehta et al. 2021). The larger sizes likely reflect the greater characteristic lengths of disc instabilities at higher redshifts (Elmegreen et al. 2008; Genzel et al. 2011, 2023). However, details of clump properties remain debated. The lack of clarity primarily stems from disagreements about the true distribution of mass, size, and ages of these structures, with observations of lensed and unlensed galaxies, as well as simulations, differing in their conclusions.

A defining feature of clumps that is agreed upon however, is their significant contribution to the total star formation of the host galaxy. In the local Universe, stars typically form within giant molecular

⋆ E-mail: boris.kalita@ipmu.jp, kalita.boris.sindhu@gmail.com
† Joint-Kavli Astrophysics Fellow.

clouds (GMCs; McKee & Ostriker 2007; Schinnerer & Leroy 2024, for reviews). However, studies of star-forming galaxies at $z > 1$ indicate the formation of giant star-forming regions due to dynamical instabilities on scales approaching the disc thickness (Elmegreen et al. 2009; Jones et al. 2010; Livermore et al. 2012; Bournaud 2016; Genzel et al. 2023). This is further supported by measurements showing the Toomre instability parameter is < 1 in regions where clumps are detected (Genzel et al. 2011).

Theoretically, clumps arising from instabilities will have their mass and size as a function of the surface density of the host discs (Ceverino et al. 2012; Livermore et al. 2012; Reina-Campos & Kruijssen 2017). The expected (and observed) sizes of these clumps can range from ~ 100 pc (or lower, e.g. Cava et al. 2018, similar to local massive star-forming H II regions) to ~ 1 kpc (Elmegreen et al. 2009; Jones et al. 2010), with the massive end requiring higher dispersion or rotation to counterbalance increased self-gravity (Dekel & Birnboim 2006; Ceverino et al. 2012; Epinat et al. 2012; Livermore et al. 2015).

The spatial resolution likely limits detection capabilities, with lensed studies detecting scales of a few hundred to tens of parsecs (Jones et al. 2010; Livermore et al. 2012; Adamo et al. 2013, 2024; Johnson et al. 2017; Cava et al. 2018; Zick et al. 2020; Messa et al. 2022, 2024a; Meštrić et al. 2022; Vanzella et al. 2022a, b; Claeyssens et al. 2023, 2024; Fujimoto et al. 2024; Mowla et al. 2024), but potentially resolving out more extended structures [depending on the signal-to-noise (S/N) ratio after magnification]. Meanwhile, unlensed studies, primarily using *Hubble Space Telescope* (*HST*), are affected by blending, and mainly detect clumps $\gtrsim 1$ kpc (e.g. Genzel et al. 2006; Förster Schreiber et al. 2011; Guo et al. 2018). Such resolution limits can lead to an overestimation of stellar masses and sizes of the clumps (Tamburello et al. 2015; Fisher et al. 2017; Huertas-Company et al. 2020).

The implication of accurate measurements goes beyond the characterization of clumps and the conditions of star formation. There is a debate regarding the survival of these structures, with some simulations suggesting that they survive up to a few 100 Myr. This inevitably leads to an inward migration into the forming bulge due to the combined effect of dynamical friction and gravitational torques (Elmegreen et al. 2007; Mandelker et al. 2014, 2017). Although, massive clumps could be sheered by the gravitational potential well if they grow larger than the Jeans length (Elmegreen & Efremov 1996). On the other hand, some works suggest that they are disrupted due to stellar feedback on very short time-scales $\lesssim 100$ Myr (Murray, Quataert & Thompson 2010; Hopkins et al. 2012, 2014; Buck et al. 2017; Oklopčić et al. 2017) and play an insignificant role in bulge formation. In either case, the bulge once formed can stabilize the disc and lead to a decrease in the formation of clumps (Martig et al. 2009; Hopkins et al. 2023; Kalita et al. 2024b).

This uncertainty could be resolved with proper measurements of clump masses and sizes across the aforementioned variety of scales. Mandelker et al. (2017) found that clumps with masses $> 10^{8.2} M_\odot$ would survive the effects of feedback, while those that are smaller would be short-lived. Krumholz & Dekel (2010) provide a division based on star formation. Clumps would be disrupted if > 10 per cent of their mass is converted to stars within their freefall time.

Recent works targeting clumps in unlensed galaxies at $z > 1$ have begun using the *JWST*/NIRCam (Near-IR camera) instrument (Kalita et al. 2024a, b). In these studies, the wide wavelength coverage is used to measure aperture-based and background subtracted clump fluxes. This however restricts the resolution to the longest wavelength band due to the need for point spread function (PSF)-matching (*F444W*; with resolution of $\gtrsim 1$ kpc at $z > 1.0$). Hence, the higher resolutions

of the shorter wavelength bands (*F115W* and *F150W*) are not fully exploited.

Use of *F115W* and *F150W* bands would lead to PSF full width half-maximum (FWHM) $\lesssim 400$ pc at $z \sim 1.5$. If clumps were detected at 3σ, one can therefore have spatial sensitivity down to about 0.1 kpc for the *F150W* filter at the target redshift of this work ($z \approx 1.5$). Therefore, physical resolutions usually achievable in lensed studies before *JWST* can now be naturally reached. In this work, the clump measurements are done using model fitting rather than apertures. This allows the extraction of fluxes through deblending even in the longer *JWST* bands with slightly broader PSFs. This method also allows us to reach spatial sensitivities down to 0.1 kpc (which is empirically verified in Section 2.4).

Throughout this paper, we adopt a concordance Lambda cold dark matter (ΛCDM) cosmology, characterized by $\Omega_m = 0.3$, $\Omega_\Lambda = 0.7$, and $H_0 = 70$ km s^{-1} Mpc^{-1}. Magnitudes and colours are on the AB scale. All images are oriented such that north is up and east is left. Use of the log-scale always refers to $\log_{10}$.

2 ANALYSIS

2.1 Sample and data

For this work, we begin with the Fiber-Multi Object Spectrograph (FMOS)-Cosmic Evolution Survey (COSMOS)-ALMA sample of 57 star-forming main-sequence galaxies[1] (within a ~ 0.5 dex scatter; Kashino et al. in preparation), with both *JWST*/NIRCam and ALMA continuum data. This is a sub-set of the spectroscopically confirmed sample of over 1500 galaxies with Hα detection in the COSMOS field (Scoville et al. 2007; Silverman et al. 2015; Kashino et al. 2019). The galaxies are within a redshift range of $1.43 \leq z \leq 1.74$ and have stellar masses of $10^{10.5-11.4} M_\odot$. Each of these has Hα and [N II] emission line detections, allowing measurements of star formation rates (SFRs), average Balmer decrements (using additonal Hβ detections and upper-limts), and metallicities (Kashino et al. 2013, 2019). Thus, we have access to metallicity dependent dust-to-gas ratios (Kashino et al. in preparation), which will be used in this work. The parent FMOS sample was selected using Hα, which introduces a potential bias toward low dust attenuation (Silverman et al. 2015). However, this works in our favour as it allows for better detectability of clumpy structures using optical bands, which is the focus of this study.

Most of these galaxies are covered by the COSMOS-Web survey (Casey et al. 2023). A total of 11 galaxies do not have coverage in all four bands due to pointing variations, which are removed from our sample. This provides us with 4-band *JWST*/NIRCam data (with average 5σ AB magnitude depths; PSF FWHM): *F115W* (27.2 mag; 0.04 arcsec), *F150W* (27.4 mag; 0.05 arcsec), *F277W* (28.0 mag; 0.09 arcsec), and *F444W* (27.9 mag; 0.14 arcsec). Each image has a pixel scale of 0.03 arcsec. The PSFs for each filter are created using the software PSFEX (Bertin 2011) on the full COSMOS-Web mosaic. We also have access to the *F814W HST*/ACS imaging (Koekemoer et al. 2007) with a 5σ depth of 27.2 mag and PSF FWHM of 0.08 arcsec. However, we find that the fitting procedure for clumps, as described in Section 2.2, becomes highly uncertain in *F814W*, which covers the rest-frame UV for our sample. This is due to a combination of low intrinsic flux (F_ν) that is not compensated by the already shallow data, along with the broader PSF compared to the adjacent band (*F115W*).

---

[1]AGN hosts are excluded in the sample selection based on broad-line data and X-ray flux.
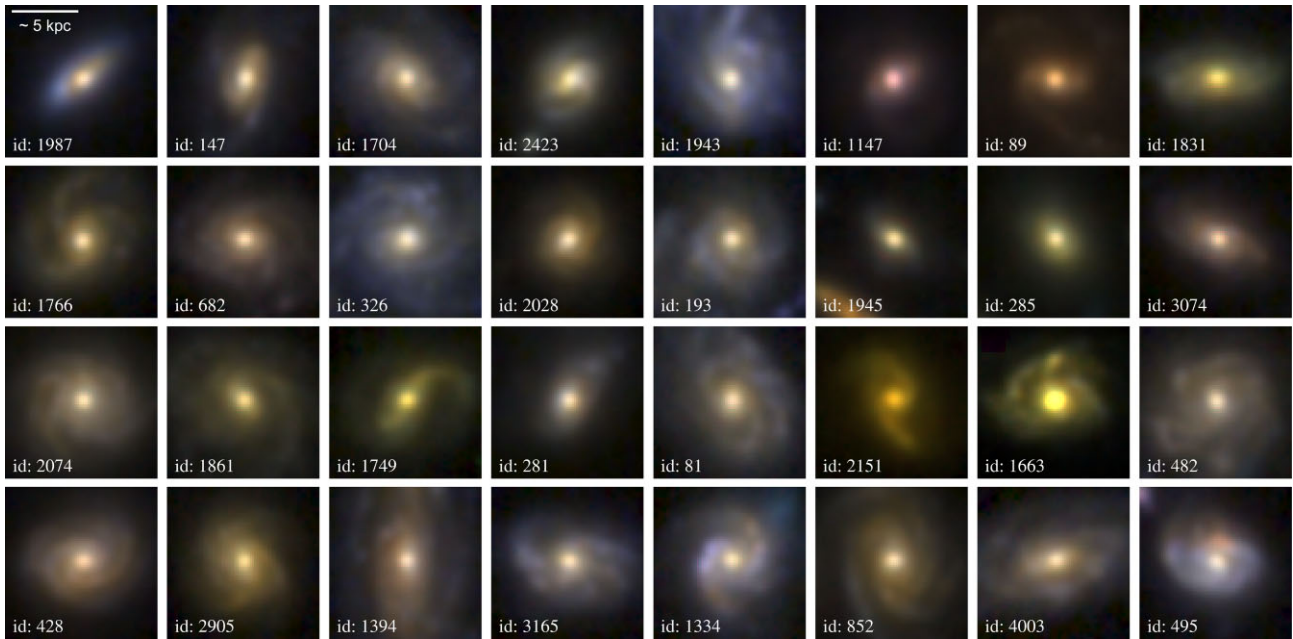
Figure 1. The three colour images (*F150W*, *F277W*, *F444W*) of the 32 galaxies used in this work have dimensions of 70×70 pix, or 2.1 arcesc $\times$ 2.1 arcesc. They are arranged in order of increasing RA and Dec. All are within a redshift range of $1.43 \leq z \leq 1.74$ and have stellar masses of $10^{10.5-11.4}$ M$_\odot$. The FMOS ID for each galaxy is provided in the bottom-left corner, with their corresponding properties listed in Table C1. The *F150W* and *F277W* images are PSF-matched to the *F444W* image using a Gaussian kernel. However, this work does not require PSF matching; it is performed here solely for illustration purposes.

In the fraction (~ 50 per cent) where we do have reliable clump flux estimates, we confirm that our results do not change with or without using this filter. Hence, we do not include it in the final analysis.

We discard any galaxies with obvious signs of (major-)merging activity by visually inspecting each of the four NIRCam images.[2] This is to ensure that we are primarily targetting clumps arising from dynamical instability in rotationally supported discs. While this is not a particularly aggressive method of assessment, we find that each of the remaining galaxies is well-fit with a single bulge + disc model in the rest-frame near-infrared (IR; further discussed in Section 2.2), supporting our assessment that the galaxies are not undergoing highly disruptive major mergers. Using the same bulge + disc modelling, we also reject galaxies with disc axes ratios < 0.5. This ensures that we study only galaxies where clump detection is not missed due to orientation, restricting our sample to nearly face-on objects. We are left with 32 galaxies, whose three colour images are shown in Fig. 1. The corresponding contrast *F150W* images, used for clump detection and shape estimation are provided in Fig. 2 (see Section 2.2 for details).

Finally, we also use the Atacama Large (sub-)Millimeter Array (ALMA) 870 μm Band-7 continuum data to characterize the rest-frame sub-mm galaxy flux. The 1σ depth is found to be ≈ 200 μJy beam^{-1} and the synthesized beam size is 0.69 arcsec $\times$ 0.57 arcsec if naturally weighted. These data were taken as part of ALMA proposal ID: 2021.1.01133.S (PI: D. Kashino). It should be noted that here we use UV-space fitting, following methods from previous works (e.g. Puglisi et al. 2019; Kalita et al. 2022; Tan et al. 2024a, b). This allows us to fit profiles that may have smaller sizes than the synthesized beam, provided the S/N ratio is sufficiently high.

2.2 *JWST* data measurements: bulge + disc + clumps

For the analysis of the images, we introduce a new method for fitting the sources, thereby 'deconstructing' the galaxies into their constituent bulges, discs, and clumps (Figs 3, 4, and 5). Based on the analysis of clumpy galaxies in Kalita et al. (2024b, b), we find that the contrast between the clump flux and the underlying disc flux increases from the rest-frame near-IR (*F277W*, *F444W*) to the rest-frame optical (*F115W*, *F150W*). This is reflected in the flux surface density contrast relative to the underlying disc (Fig. 6). This effect can be attributed to two factors: (i) the near-IR traces older stellar populations, thereby mapping the average stellar mass distribution rather than star formation (which is higher in clumps), and (ii) the resolution of these longer wavelength bands being a factor of $\gtrsim 3$ lower than that of the shorter wavelength ones. For the same reasons, the rest-frame near-IR is effective at mapping the underlying bulge and disc (Sheth et al. 2010).

We employ a two-stage spatial model-fitting procedure that optimizes the bulge and disc models using the *F444W* filter and the clump models using the *F150W* filter. We choose to use *F150W* for clump detection instead of *F115W* due to the latter's shallower depth and possible biases from an undersampled PSF. We start by fitting a dual-Sérsic profile with indices 2 and 1 for the (pseudo-)[3] bulge and disc, respectively, in the *F444W* filter.

Following this, clump modelling is performed by first detecting these structures in the contrast images which are shown in Fig. 2 (following procedures presented in Kalita et al. 2024a, b). These are created by smoothing the image with a Gaussian kernel with $\sigma = 3$ pix, and then subtracting it from itself. The detection is done in stages using incrementally lower σ thresholds to find regions of

---

[2]However, the sample galaxies might be experiencing minor-merging activity, which cannot be identified visually.

[3]We ensure that using a classical bulge with a Sérsic index $= 4$ does not change our results. However, we use the value for a pseudo-bulge since the central region is star-forming throughout our sample.
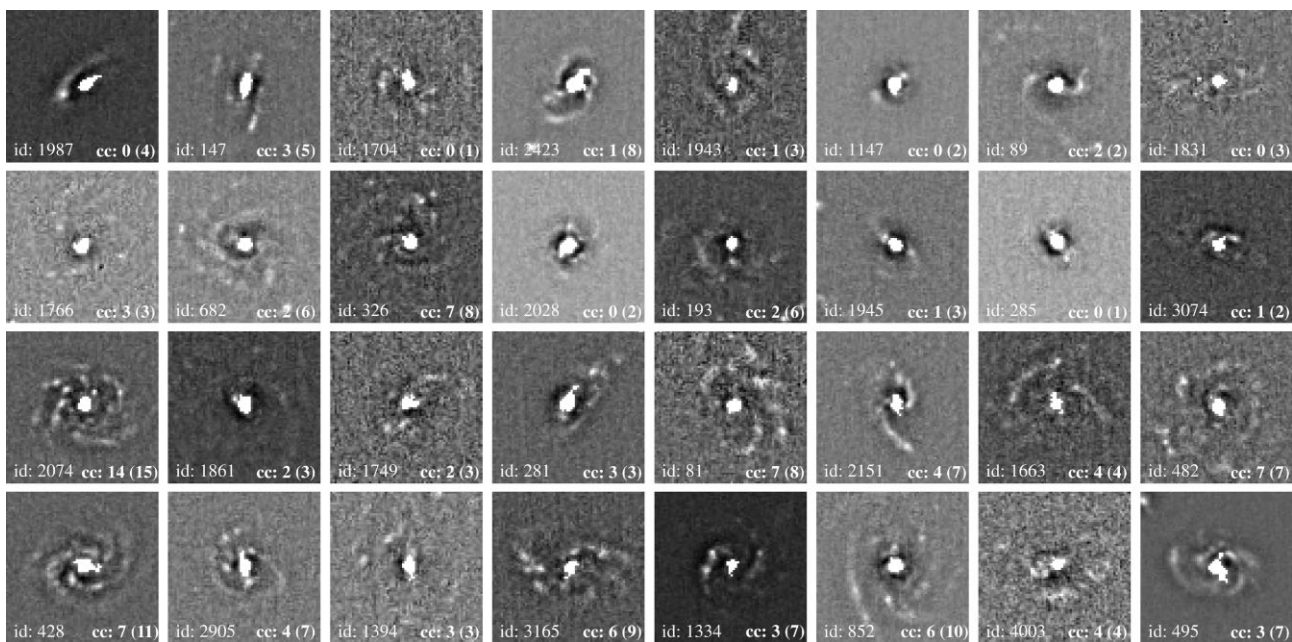
Figure 2. The contrast images created from the *F150W* images, by subtracting a smoothed version of themselves, for the 32 galaxies in our sample (three colour images shown in Fig. 1). These are used to detect clumps. In each galaxy, we have also added the final number of detected clumps (clump counts, or cc), along with initial number of clumps, shown in brackets, before the rejection based on the reduced-χ^2 of their respective SED fits.

progressively fainter flux peaks. At each stage, the detected clumps are fit with elliptical Gaussian models, along with the existing bulge + disc model from the first stage. As clumps are progressively added, increasing the model's complexity, we simultaneously measure the Bayesian Inference Criterion (BIC) at each step. This allows us to evaluate the trade-off between the goodness-of-fit and the model's complexity. For each galaxy, the lowest BIC values are reached at either 3σ or 4σ threshold.

The final bulge + disc + clump spatial models (Figs 4 and 5) are fixed (i.e. their respective shapes) and are used, together with their respective PSFs, for deblending all four *JWST*/NIRCam filters for the final flux measurements.[4] Further details of the procedure, along with caveats, are provided in Appendix A. Finally, uncertainties for all flux values are calculated by artificially adding sources of the same size but varied flux values as part of composite models and then remeasuring them. This process is conducted separately for each filter. We then repeat the procedure for size measurements, fixing the flux and varying the sizes. Given that clump size measurements are performed only in the *F150W* filter, other bands are excluded from this part of the analysis. The levels of uncertainty for *F150W* flux and sizes can be found in Fig. A2.

The photometry is passed on to the Spectral Energy Distribution (SED) fitting process to derive physical parameters (described briefly in the next section). Based on the BIC values of the fits at different stages, we conclude the following:

(i) Rest near-IR: all 32 galaxies are better fit (BIC-based, accounting for model complexity) with a bulge + disc model in the rest-frame near-IR (*F444W*) compared to a single Sersic fit. However, adding

clumps to the model results in a significant improvement in the BIC ($> 10^3$) for all galaxies.

(ii) Rest optical: the bulge + disc model derived from the rest-frame near-IR does not fit the galaxies well in the rest-frame optical (*F115W* and *F150W*) due to the dominant presence of clumps in these images. However, adding the clumps to the model results in a substantial improvement in the BIC values ($> 10^5$). The improvement can be attributed to the fraction of the galaxy optical flux contained in the clumps ($\sim 5 - 30$ per cent). Thus, the bulge + disc + clump models significantly outperform the bulge + disc models in the rest-frame optical.

(iii) All bands: the final comparison of the reduced-χ^2 values across all four NIRCam images shows the trend: $\chi^2_{F115W} < \chi^2_{F150W} < \chi^2_{F277W} < \chi^2_{F444W}$, with lower reduced χ^2 values indicating a better fit. We do not use the BIC values for this comparison since the same model is used for all bands. The increasing reduced χ^2 with wavelength is likely related to residuals in the near-IR, where we clearly detect underlying stellar sub-structures that resemble spiral arms in most cases. We discuss their relevance later in Section 3.5 and 4.4. Finally, the shallower depth of the *F115W* image in comparison to that of *F150W*, along with the higher relative the contrast between the clumps and the disc (Fig. 6), and the higher resolution likely resolving out extended residual sub-structures, results in lower reduced χ^2 in *F115W*.

2.3 ALMA data measurements: bulge + disc

The second part of the analysis uses the same principle of galaxy image deconstruction on the ALMA 870 µm image. Given that synthesized beam size of ~0.6 arcsec, we find that the S/N ratio of the clumps is insufficient for accurate measurements. Therefore, we do not measure the 870 µm flux for individual clumps. However, it is sufficient for robust flux measurements of the bulge and disc through deblending (details are provided in Appendix B). Since we

---

[4]In Kalita et al. (2024a), a background was subtracted, which was estimated using the underlying disc flux at the relevant radial distance from the centre while excluding the clumps. However, this is not necessary here since we are simultaneously modelling the clumps and the underlying disc.
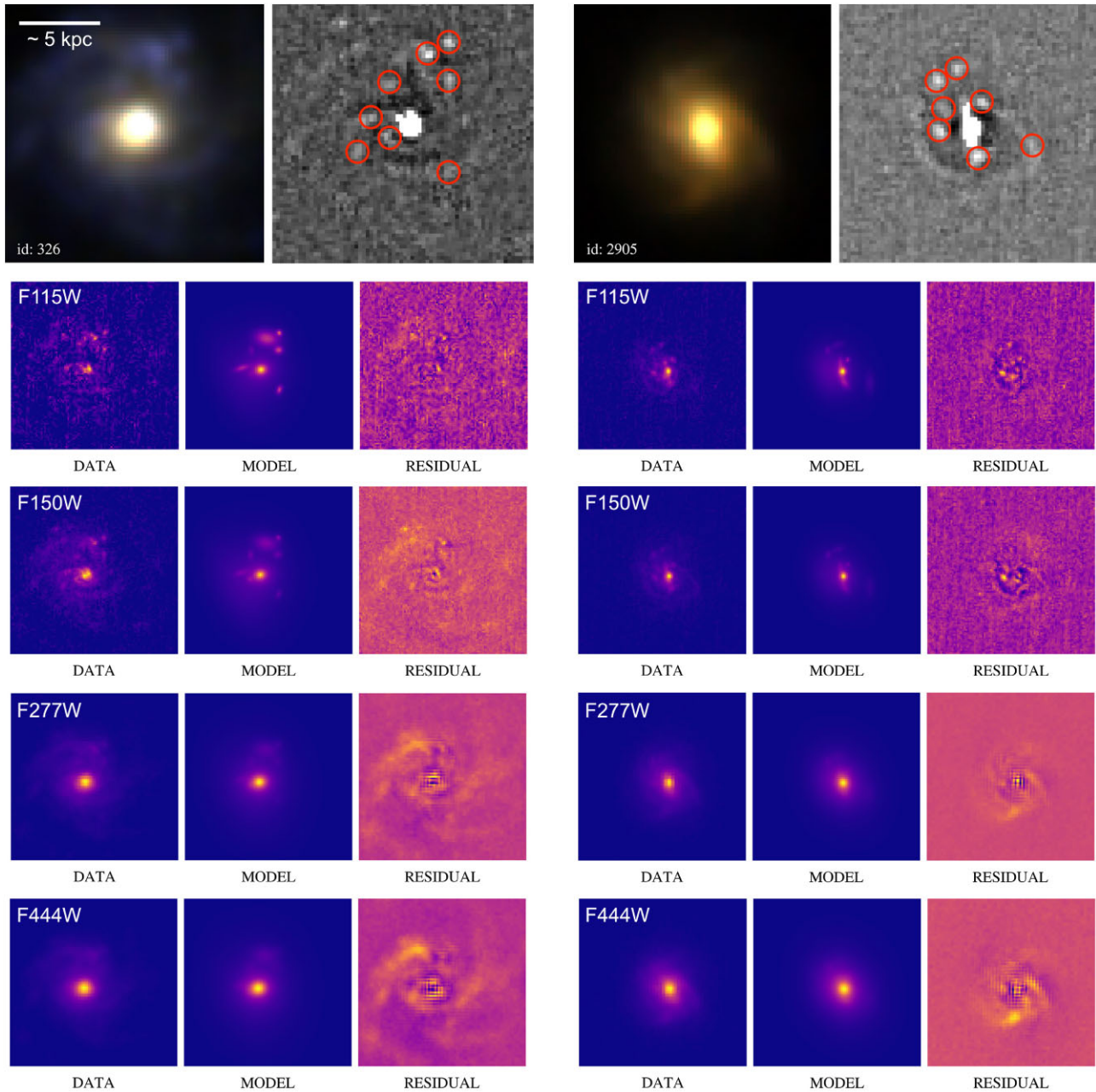
Figure 3. The 'deconstruction' of 2 of the 32 galaxies in our sample. The three colour image of each galaxy (Fig. 1) is shown at the top left. Next to it is the *F*150*W* contrast image (from Fig. 2) used to detect the clump locations (initial number of clumps), marked in red. Each clump is associated with a Gaussian model. Below, the corresponding data, model, and normalized residual (data-model/noise) for each *JWST*/NIRCam image are provided. Note that the colour image is created by PSF-matching the *F*150*W* and *F*277*W* images to the *F*444*W* image, while the deconstruction is done at the native resolution of the respective filters.

do not deconvolve the clumps here, the disc flux includes the clump contributions.

We use the bulge + disc model derived from the *F*444*W* rest-frame near-IR image, with the position and shape fixed, to extract the 870 μm flux. This is done by translating the image plane parameters to the UV-plane (using values from Tan et al. 2024b) and then measuring the flux of each (fixed) component. We use this approach because the ALMA data does not have sufficient S/N ($> 50\,\sigma$) for robust shape measurements (Tan et al. 2024b). Here, we assume that the stellar light and dust emission are coincident, which has been supported by recent studies (Hodge et al. 2024; Liu et al.

2024). Tan et al. (2024a) also concludes that part of the sub-mm flux can be attributed to the star-forming, under-construction bulge. Using the bulge + disc model allows us to determine the bulge and disc contributions to the total 870 μm flux from the galaxy.

We compile the bulge and disc photometry using the four *JWST*/NIRCam bands and ALMA Band-7. The disc flux in the NIRCam bands includes the flux of all clumps within the 90 per cent flux radius (r_{90}) of the disc; any flux beyond this radius is not considered. A similar approach is unnecessary for ALMA, as we deblended the data using only a bulge + disc model that includes
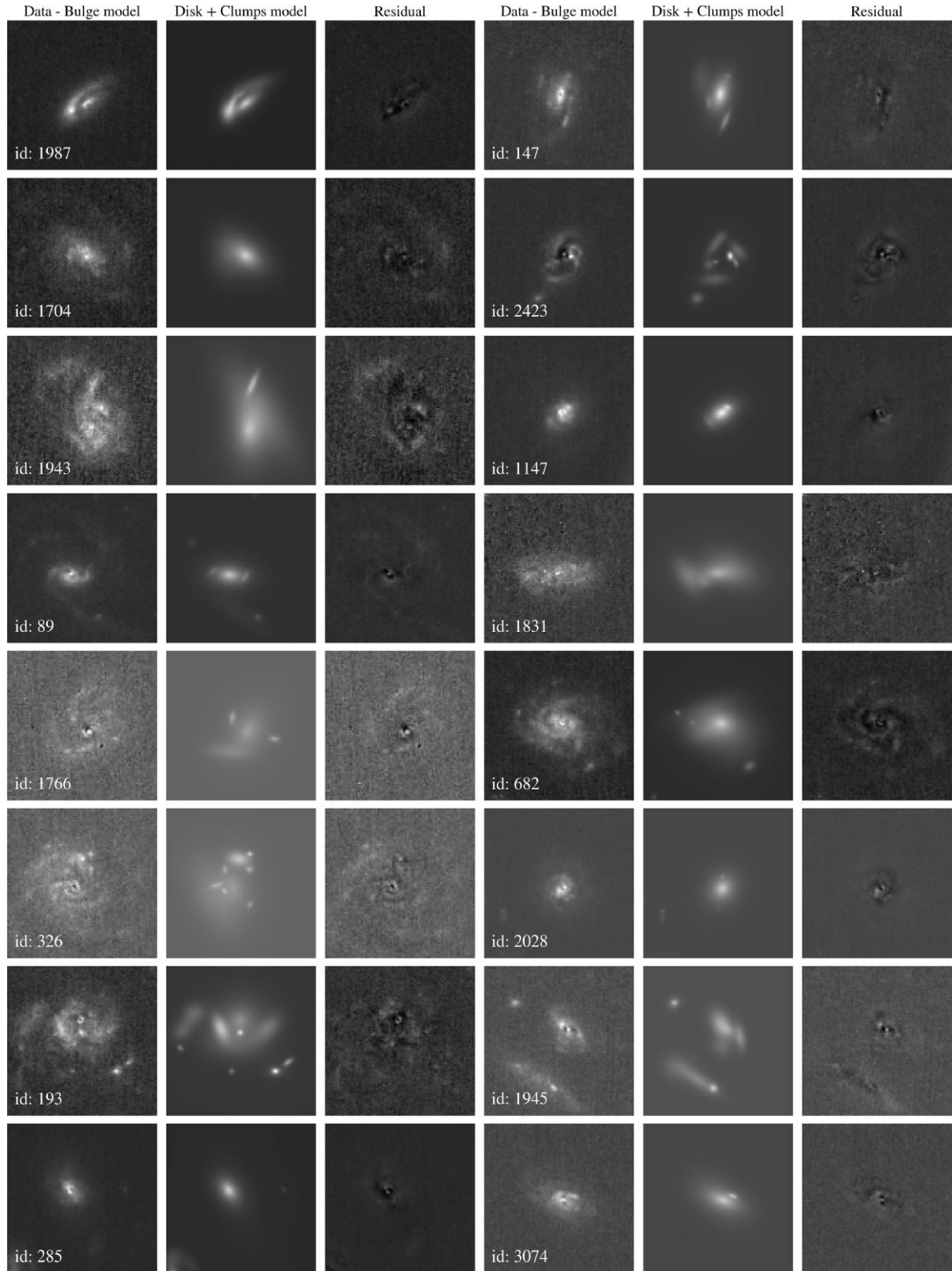
Figure 4. (Data–bulge model) The *F*150*W* image of the clumpy discs, after the subtraction of the bulge model for 16/32 galaxies in our sample. (Disc + clumps model) The corresponding model image, that includes the disc and all initially found clumps, without the bulge. (Residual) The final residual image after the subtraction of all the model components from the data.
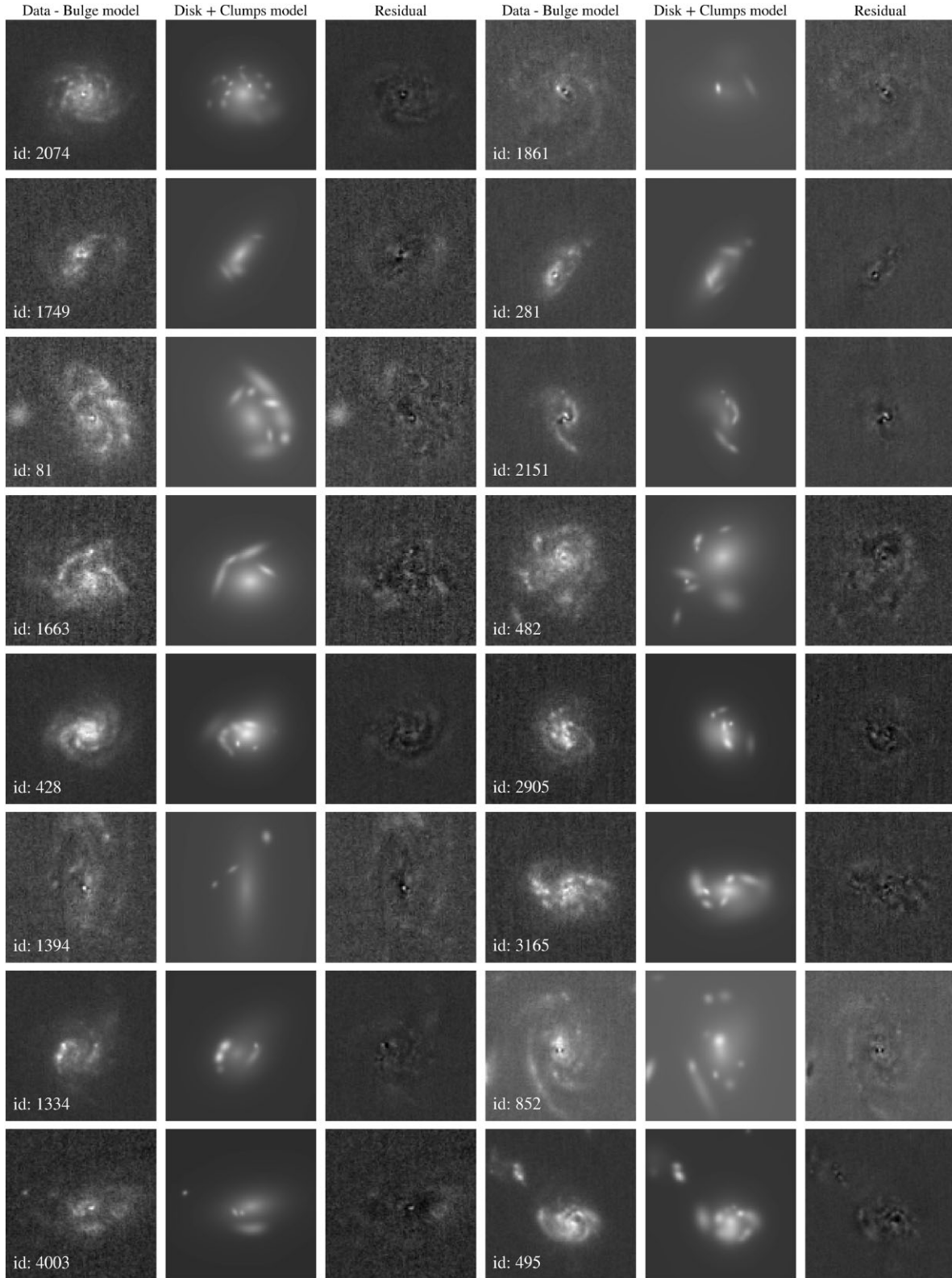
Figure 5. The same images as in Fig. 4 for the remaining 16/32 galaxies.

any clump flux. These flux measurements are then used in an SED analysis (Appendix C) to calculate physical properties such as stellar mass and SFRs. The analysis uses constant star formation history models to fit the 5-band photometry for the bulge and disc of

each galaxy using the PYTHON based 'Code Investigating GALaxy Emission' (CIGALE; Boquien et al. 2019) tool. The clump SED fitting relies only on the four *JWST* bands, as their ALMA Band-7 flux is unavailable. The 1σ errors in the measured parameters are based
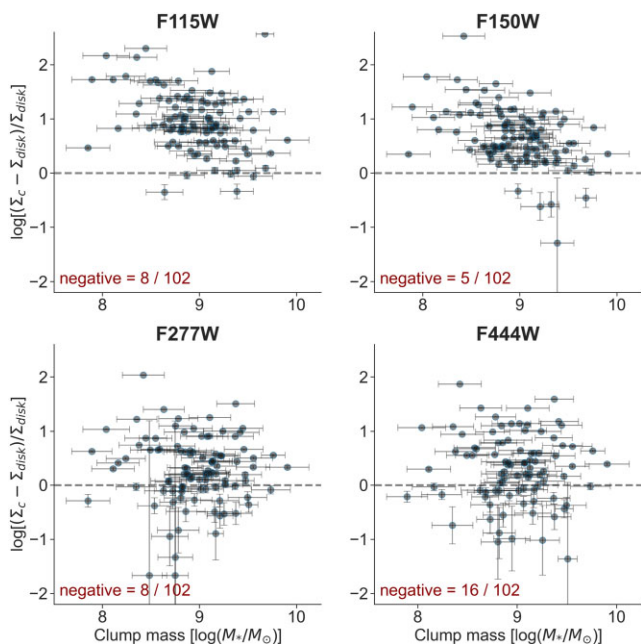
Figure 6. The surface brightness contrast between the clumps (detected in *F150W*) and the rest of the host disc in different filters as a function of their stellar mass. In some cases (termed 'negative'), the surface brightness is lower than the disc's average, which is possible since their detection depends on the local flux distribution around the clump region. Notably, the number of such clumps is higher in the rest-frame near-IR (*F277W* and *F444W*) compared to the rest-frame optical (*F115W* and *F150W*).

on the $\Delta\chi^2 = \pm 1$ of their respective distributions as reported by CIGALE.

We already have the integrated dust mass of the galaxies from the 44-band (rest-frame UV to far-IR COSMOS data; Weaver et al. 2022) SED fitting, which is converted to gas mass using metallicity dependent dust-to-gas ratios (to be presented in Kashino et al. in preparation). Assuming similar SEDs for the bulge and disc, we use the ratio of the 870 µm fluxes to estimate the gas mass of the bulge and disc. These values will be used later in Section 3.1.

2.4 Detection completeness and uncertainties

The first test of the robustness of the analysis is whether we account for the total stellar mass and SFR of the galaxies. We therefore compare the total stellar mass and SFR of the bulge and disc of each galaxy (the latter also including the clumps) to the integrated values for the galaxies presented in Kashino et al. (in preparation). They use a similar SED fitting set-up as in our work (mentioned in Section 2.3 and details in Appendix C) but have additional access to the full wavelength coverage of the COSMOS field (Weaver et al. 2022). We find agreement for the SFR values within the errors, while there is, on average, a 0.1 dex offset in stellar mass, with our values being lower (Appendix C and Fig. C4). We attribute this to the use of 3 arcsec apertures in Kashino et al. (in preparation), which are characteristically larger than the extent of our galaxy model (the measured disc r_{90} is on average ~1.5 arcsec). However, it should be noted that we miss some flux within the galaxies in the longest bands, which appears in the form of spiral arms in the residuals. Exactly estimating the flux in these residuals is challenging since they contain both positive and negative flux values due to oversubtraction and undersubtraction at different locations.
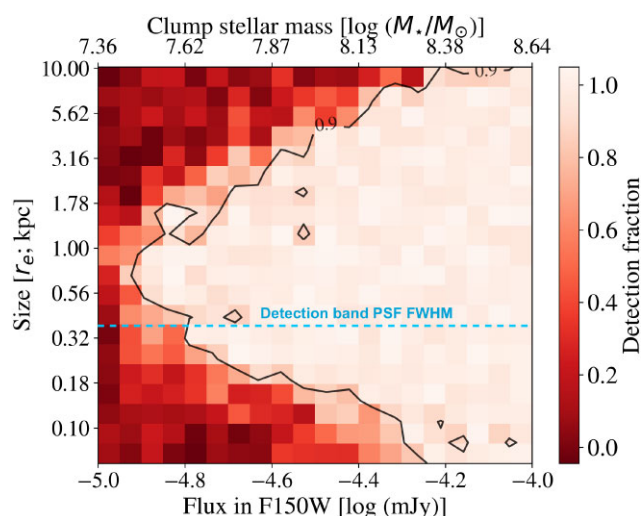

Figure 7. The completeness of our detection algorithm as a function of clump *F150W* flux (detection filter) is shown on the bottom *x*-axis, and clump size (r_e). The corresponding clump mass is computed using the average mass-to-light ratio of our clump sample and displayed on the right as a function of size on the top *x*-axis. The physical size of the PSF (FWHM) of the detection image (*F150W*) is also indicated in using a dashed line.

The detectability of the clumps in the galaxies would likely depend on their intrinsic flux and size, which contribute to the contrast with the underlying disc. We therefore artificially add clumps to the galaxies in the corresponding *F150W* image, spanning a reasonable range of fluxes and sizes, and attempt to detect them using the same procedure as discussed in Section 2.2. We randomly place these clumps over the surface of the disc (up to the r_{90}) while ensuring they do not fall within the bulge region.[5]

We consider a clump as detected if the procedure finds a new source within the effective radius of the artificial clump. This gives us the detection completeness of our procedure as a function of *F150W* flux and size (Fig. 7, bottom *x*-axis). We carry out this procedure for each galaxy, with the final result representing the average across the full sample. It is worth noting that we do not refit the artificially added clumps if they are detected. This decision is made because the accuracy of the fitting procedure in extracting correct flux and size measurements depends not only on clump properties but also on variations in the underlying disc flux. Thus, error quantification is performed for each clump and has been discussed in Section 2.2. The goal of determining completeness here is simply to gain a general understanding of clump detectability in our study.

Since we already measure the stellar mass of the clumps in our sample, we estimate a mass-to-light ratio[6] from the corresponding *F150W* flux measurements (relation shown in Fig. C3). We then use this to estimate completeness in terms of size and stellar mass (Fig. 7, top *x*-axis). It is worth noting that the flux-to-stellar mass conversion is accurate only up to the uncertainty of the SED-based stellar mass estimation, which is on average ~ 0.35 dex. However, the uncertainty of the representative conversion for the full clump

---

[5]It is challenging to determine the exact extent of the bulge to ensure the artificial clumps are not placed within it. We use the segmentation map in *F150W*, which is used to detect the real clumps. Here, the bulge is also detected as a clump, which is usually rejected in our analysis. However, the associated segmentation region provides an estimate of the bulge's extent.

[6]$\log(M_\star) = (\log(\text{flux}) + 10.74 \pm 1.94)/(0.78 \pm 0.21)$.

sample would also depend on the deviation of the mass estimates from the average ratio (Fig. C3). Hence, we settle on a conservative uncertainty of 0.5 dex. For the smallest clumps (~ 0.1 kpc) with a completeness flux limit of $\log(\text{Flux}_{F150W\,|\,\text{mJy}}) = -4.3$ we therefore find a resulting stellar mass limit of $\approx 10^{8.7}\,\text{M}_\odot$. The additional 0.5 dex improves our completeness estimation by addressing the previously unaccounted robustness of the flux extraction. These uncertainties are also similar to the systematic variation we might expect in clump mass measurements as a function of galactocentric radius (~ 0.35 dex that is estimated in Kalita et al. 2024a). Hence, clump detection completeness has not been characterized as a function of radial distance from the centre in this study.

The resolution of the *F*150*W* image (FWHM ~ 0.4 kpc at $z \sim 1.5$) influences the detection completeness of the clumps. However, we detect and measure clump sizes down to ~ 0.1 kpc due to the high S/N of these structures. Given that we are fitting models, we can therefore characterize sub-PSF scales (as mentioned in Section 1), albeit with relatively higher uncertainties. This effect can be observed in Fig. 7, where the smallest clumps can be detected only when their flux (and hence S/N) is high. Nevertheless, throughout the work, we ensure that our results are valid regardless of whether we include or exclude the sub-PSF clumps.

Another key feature of Fig. 7 is the decrease in detection fraction for the largest sizes. This is primarily due to the flux being spread over a larger surface area, which reduces the S/N ratio of each pixel, making detection more challenging. Additionally, this characteristic, observed above a few kpc, is due to the clump sizes approaching those of the galaxy discs, which have a 90 per cent flux radius of $\sim 5 - 10$ kpc. Such clumps would not be identified as localized flux increments necessary for detection. Meanwhile, the smallest clumps may go undetected if they have low flux, as they are excluded by the detection algorithm when detected over < 5 pix. This criterion is implemented to reject noise peaks. The decreasing completeness limit below the PSF size of ~ 0.4 kpc, as evident from Fig. 7, is a result of this rejection.

Finally, one caveat of our procedure that must be noted is the complex structure of clumps, which we attempt to fit using a Gaussian model. The goal is to capture the most dominant structure in terms of net flux, which would be represented in the final best-fit model. However, in multiple cases, we observe that the residuals still contain smaller sub-structures not accounted for by the clump models. Ideally, we would add additional models at the locations of these sub-structures, in addition to the primary clump model. However, this approach often results in a failure to converge or no improvement in the final BIC. Therefore, we acknowledge this as a limitation that cannot be resolved within the scope of our data and procedure.

3 RESULTS

3.1 Galaxy properties

Here, we briefly mention a few key results from the bulge and disc model-based measurements. The current study focuses on the clumps within the galaxies. Discussions of global properties, central regions, and bulge–disc properties will be provided in forthcoming works. We find that the galaxies span a stellar mass range of $10^{10.6-11.2}\,\text{M}_\odot$ and an SFR of $50 - 200\,\text{M}_\odot\,\text{yr}^{-1}$ (Fig. 8). As mentioned in Section 2.2 and Appendix A1, each galaxy is well-fit by a bulge–disc model (and better than a single Sersic, after accounting for model complexity). This suggests that our sample consists of galaxies with a clear disc and, to varying degrees, a bulge. Major mergers have thus been
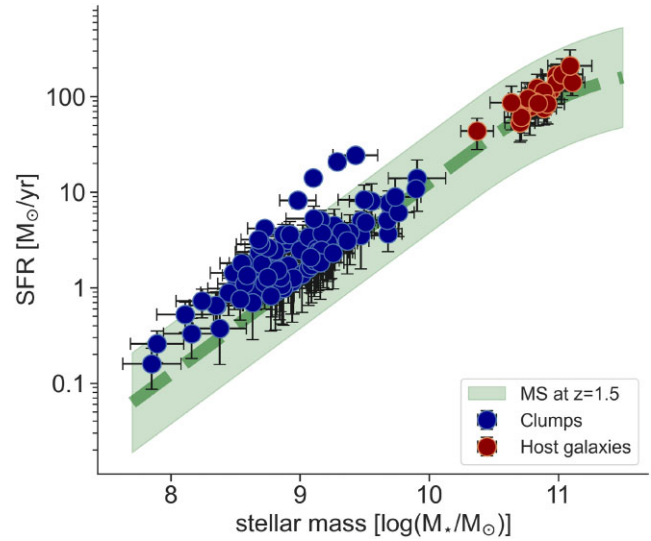

Figure 8. The SFR versus stellar mass relation of the clumps in our sample, along with that of the host galaxies, is shown. For reference, the star-forming main-sequence at $z = 1.5$ (Schreiber et al. 2015), with a ± 0.3 dex scatter region, is also provided. All clumps are found to lie within the scatter of this relation, though generally above the average. Meanwhile, the hosts, originally selected to be within the main-sequence, unsurprisingly follow the relation more closely.

excluded (Section 2.1). The bulge-to-disc stellar mass ratio ranges from 0.1 to 0.6.

In each case, the net star formation in the disc is higher than in the bulge, likely fuelled by molecular gas contents, characterized by disc gas fractions ($f_g = 0.1 - 0.8$). These are estimated using the 870 μm flux based estimations of gas mass discussed in Section 2.3. However, among the 26 galaxies featuring clumps, the minimum f_g is 0.36. Finally, the disc mass surface density, $\Sigma_{\text{disc}} = 10^{8.3-9.3}\,\text{M}_\odot\,\text{kpc}^{-2}$, accounts for the contribution of both the gas and the stellar mass in the disc.[7]

3.2 Clump properties

The model-fitting technique we employ allows us to measure the clump fluxes and sizes,[8] along with their associated uncertainties and completeness limits. Across the sample of 32 galaxies, we detect a total of 167 clumps. In order to exclude interlopers, this number does not include any sources that might have been detected beyond the rest-frame near-IR 90 per cent flux radius of the disc, which is taken from the bulge–disc decomposition discussed in Section 2.2. Only 102 of the clumps have reduced-χ^2 values < 4 of their SED fits. We discard the rest due to the unreliability of their measured properties[9] but still investigate them to ensure none of our key results change if they are included. We will mention them throughout the paper whenever relevant.

Within this final sample, the clump stellar masses vary within $10^{8.0-9.5}\,\text{M}_\odot$ (Fig. 9) with an average uncertainty of ~ 0.35 dex (1σ

---

[7]Estimated using the ratio of $0.9\times$ stellar $+$ gas mass and $\pi \times r_{90}^2$.

[8]We use the major-axis value in order for projection effects to not influence our results.

[9]The specific value of reduced-$\chi^2 = 4$ is chosen as a cut-off since beyond this we find the SED based stellar mass uncertainty to suddenly change from a consistent ~ 0.35 dex to > 0.5 dex.
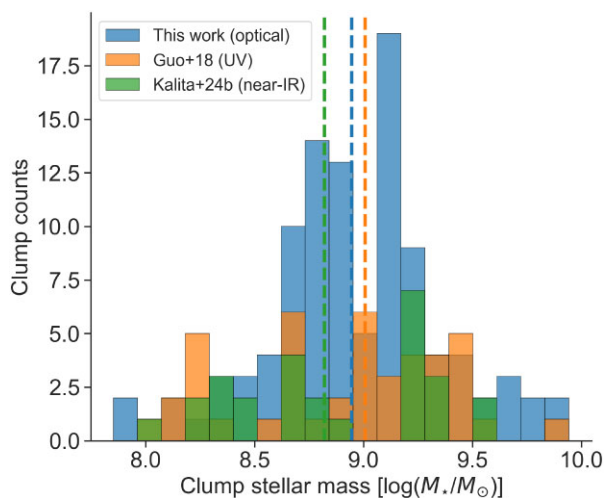
Figure 9. The distribution of stellar mass of the clumps in galaxies falls within the stellar mass range of our sample ($10^{10.5-11.4}$ $M_\odot$). For comparison, we also show the same for clumps from two previous studies that provide statistical assessments of clumps in stellar mass complete samples of galaxies (Guo et al. 2018; Kalita et al. 2024a). The former selects clumps in the rest-frame UV, while the latter does so in the rest-frame near-IR. The median values for each data set are also shown as dashed lines.
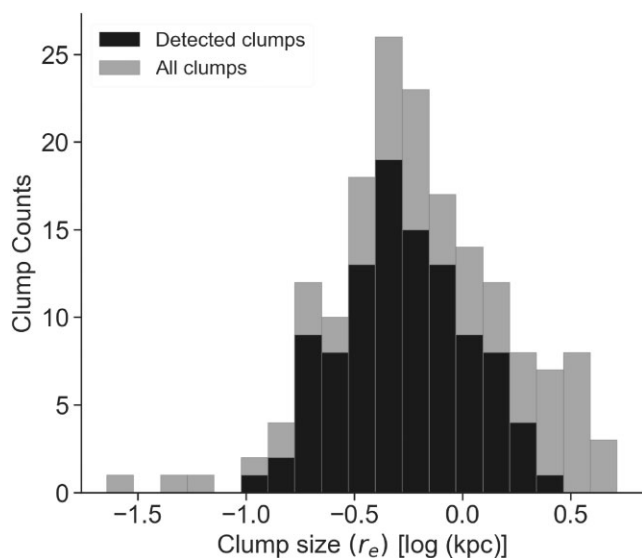

Figure 10. The distribution of clump sizes within our sample. The 'detected clumps' refer to the clumps we include in our study, while 'all clumps' also include those that have been removed due to a reduced-$\chi^2 > 4$.

uncertainties based on $\Delta - \chi^2 = \pm 1$). Meanwhile their half-light radii (r_e) ranges from ~ 0.1 to ~ 2 kpc (Fig. 10). We also confirm that the parameter space covered by these clumps is within the 90 per cent completeness limit of our detection procedure (Section 2.4; Fig. 7). Finally, we find attenuation values $A_V \lesssim 0.6$ mag and half-mass ages $\lesssim 700$ Myr[10] (the time since the formation of half the stellar mass), reflecting our detection in the rest-frame optical. However, the current data do not provide sufficient accuracy to measure these parameters

[10]Using the upper limit of the 68 per cent confidence interval.

more precisely and hence do not make any scientific claims based on these values.

The final 102 clumps are distributed among 26 of the 32 galaxies in our sample. Three additional galaxies also have detected clumps, but the SED fitting does not return fits with reduced-$\chi^2 < 4$. This high fraction of clumpy galaxies is not consistent with previous studies (~ 40 per cent e.g. Guo et al. 2015; Kalita et al. 2024a), even after accounting for the difference in methodology.[11] We attribute the higher clumpy fraction to our SFR (Hα) based selection. Galaxies below the main-sequence, heavily dust-obscured and compact (e.g. Elbaz et al. 2018; Gómez-Guijarro et al. 2018), or bulge-dominated and therefore less clumpy (Kalita et al. 2024b), would not be included in our sample.

We find that the SFR and stellar mass of the clumps are tightly correlated, consistent with the extrapolation of the star-forming main-sequence (Fig. 8, with the main-sequence from Schreiber et al. 2015). Although there is a tendency towards higher SFR values, they are generally within 0.4 dex scatter of the relation. This characteristic is evident in the increased specific SFR (sSFR = SFR/$M_\star$) compared to the host galaxy (Fig. 11, right) where we find $0 \lesssim \Delta \log$ sSFR $\lesssim 0.4$. Meanwhile, individual clumps contribute 0.1–10 per cent of the stellar mass and 0.2–30 per cent of the SFR of their hosts (Fig. 11, left and middle panels; in agreement with previous works, e.g. Wuyts et al. 2012; Kalita et al. 2024a). The total contributions from clumps per galaxy are found to be uniformly distributed over 0.5–20 per cent and 1–30 per cent, respectively (Fig. 12). It should be noted that clumps rejected due to high-χ^2 in SED fitting are not included, so the actual contributions could be higher.

We compare the clump stellar masses to Guo et al. (2018) and Kalita et al. (2024a), as these provide the largest samples in recent literature with SED measurements (Fig. 9). Only galaxies within our sample's stellar mass range are included ($10^{10.5-11.4}$ $M_\odot$). While we agree on the limits, we find a relatively large number of clumps with stellar masses around $\sim 10^9$ $M_\odot$. However, we do not make any claims about the mass distribution due to our small sample size of 32 galaxies. Both studies indicate that higher mass galaxies host higher mass clumps (also suggested by Dessauges-Zavadsky et al. 2017; Claeyssens et al. 2024), potentially reflecting clump mergers that form more massive clumps. This process could lead to a hierarchical distribution of clumps across various masses.

With the measured sizes discussed in Section 3.3, we estimate the SFR surface densities,[12] $\Sigma_{SFR} = 10^{-2} - 10^2$ $M_\odot$ yr^{-1} kpc^{-2} (Fig. 13). These values are higher than those expected in local galaxies, where Σ_{SFR} may vary between $10^{-4} - 10^{-1}$ $M_\odot$ yr^{-1} kpc^{-2} (e.g. Bigiel et al. 2008; Leroy et al. 2008; Rahman et al. 2012). However, such values are reached in the integrated Σ_{SFR} of starbursts (e.g. Kennicutt & De Los Reyes 2021), although it is unclear if the same applies to individual clumps within these galaxies (Hinojosa-Goñi, Muñoz-Tuñón & Méndez-Abreu 2016). Meanwhile, lensed galaxy samples and local high-z clumpy galaxy analogues show

[11]These works do not use the rest-frame optical bands for clump detection. Nevertheless, we find that variation of detection bands is far from sufficient to explain the factor of ~ 2 increase in the fraction of galaxies hosting clumps. Furthermore, the resolution at which the clumps are detected is lower by a factor of ~ 2. Guo et al. (2015) also has the additional requirement of a clump needing to have > 8 per cent of the Galaxy UV flux. Incorporating these, but relaxing the reduced-χ^2 cut-off we introduce still results in 25/32 galaxies being identified as clumpy.

[12]Calculated using the total SFR of the clumps and dividing by πr_{90}^2. Here, r_{90} is the 90 per cent *F*150*W* flux radius of each clump, estimated as $1.67 \times r_e$, assuming the clumps have a Gaussian profile.
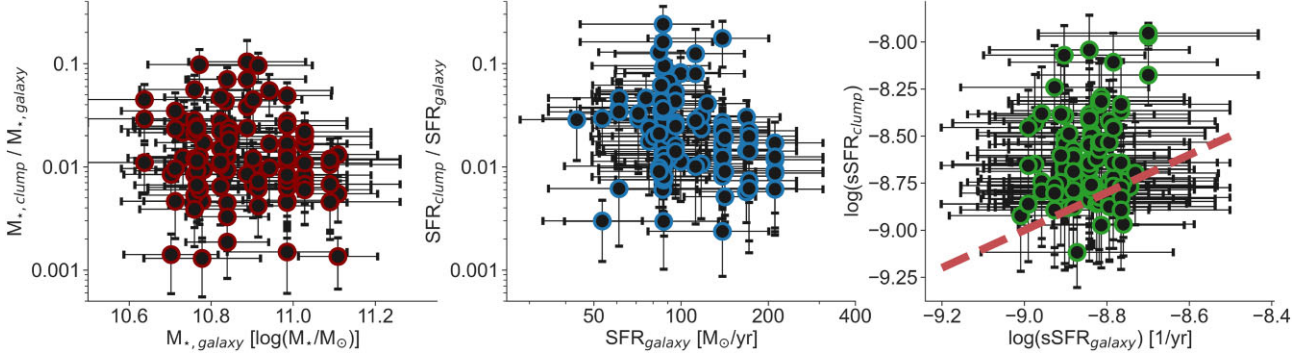
Figure 11. (Left) The ratio of stellar mass within each clump to that of the host galaxy as a function of the host's stellar mass. (Middle) The same ratio, but for SFR. (Right) The sSFR of the clumps versus that of the host. The dashed line indicates where clumps would lie if they had the same sSFR as their respective hosts; almost all of our sample is found above this line.
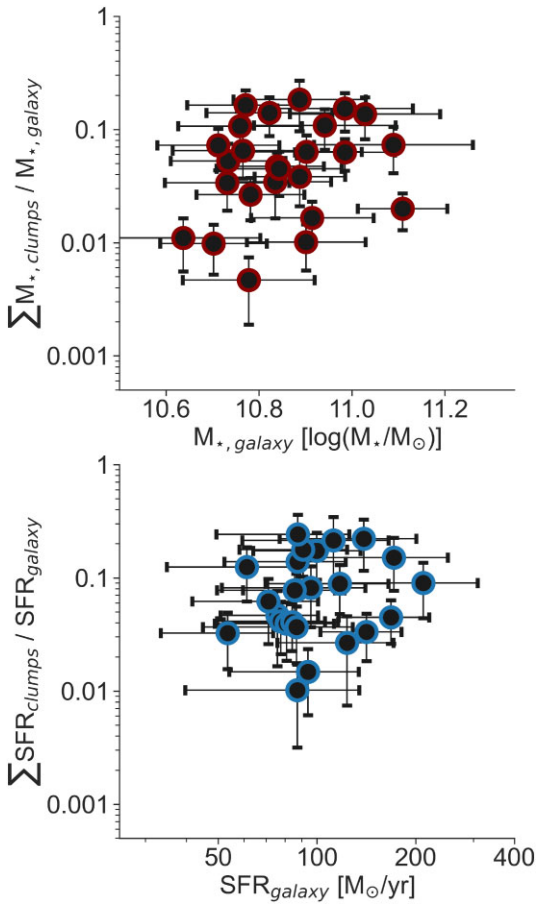

Figure 12. (Top) The ratio of the total stellar mass in the modelled clumps of a galaxy to that of the host galaxy. (Bottom) The same ratio for SFR.

similar ranges as our sample (e.g. Livermore et al. 2012; Fisher et al. 2017; Claeyssens et al. 2024; Messa et al. 2024b). High-resolution ALMA studies of high-z starbursts have also found comparable values of Σ_{SFR} (Sharda et al. 2018).

3.3 Clump mass–size relation

To relate the stellar mass and sizes of the clumps in our sample, we need to ensure that it is estimated within the completeness limits of our procedure. For clump size ~ 0.1 kpc, we have already determined
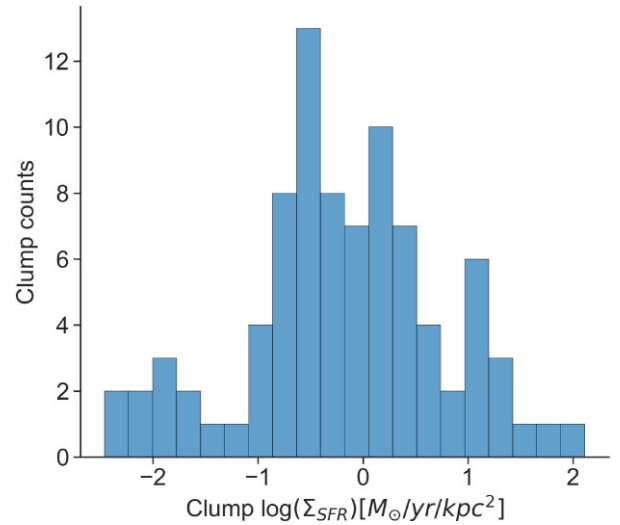

Figure 13. The clump SFR surface density ($\Sigma_{SFR} = SFR/\pi\, r_{90}^2$) distribution for our sample.

a conservative stellar mass limit of $10^{8.7}\,M_\odot$ (Section 2.4). However, for the purposes of deriving a relation, we exclude clumps with r_e below 0.2 kpc that also allows for the inclusion of clumps down to a stellar mass of $10^{8.3}\,M_\odot$ (Fig. 7, with the additional mass estimation uncertainty of 0.5 dex based on Fig. C3). Thus, using the half-light radius and stellar mass of the clumps within this parameter space, we find the best (Markov chain Monte Carlo based) fit relation to be:

$$\log(r_e[\text{kpc}]) = 0.52\,(\pm 0.07)\ \log(M_\star[M_\odot])\ -\ 4.98\,(\mp 0.55). \quad (1)$$

Given observational limitations, it is possible that random groupings of smaller, unrelated clumps observed together due to projection effects may influence this relation. However, we argue against this scenario in Sections 4.1 and 4.2 based on theoretical expectations. We instead conclude that clumps at all scales are coherent, with smaller undetected sub-clumps (with masses $< 10^{8.0}\,M_\odot$ and sizes < 0.1 kpc) being part of a hierarchy of structures.

We also examine whether including the clumps that were excluded due to a high reduced-χ^2 affects our results (grey points in Fig. 14). We find that the slope of the relation then becomes 0.49 (± 0.08), and the constant changes to 5.32 (∓ 0.63). Thus, excluding clumps based on reduced-χ^2 does not significantly change our results. Furthermore, we conclude that the excluded clumps are mainly those
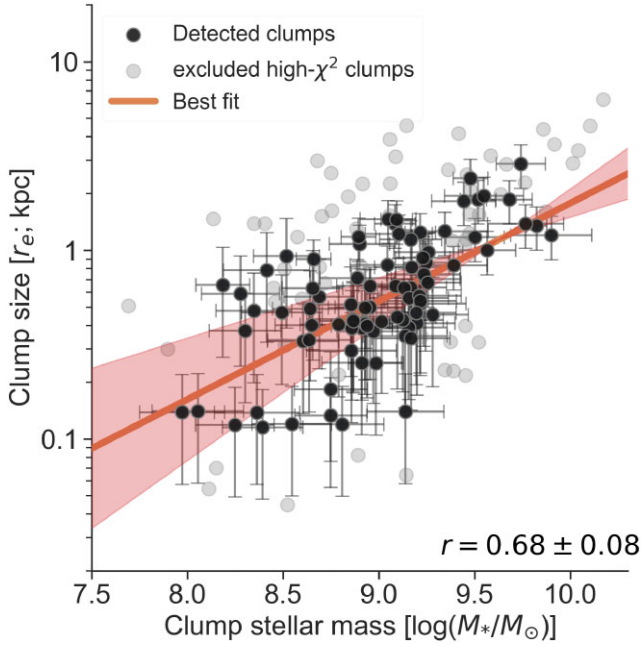
Figure 14. The clump mass–size distribution for our sample, along with the best-fit relationship. The correlation coefficient is 0.68 ± 0.08, with the error estimated through bootstrapping. The high value (> 0.5) indicates a strong correlation. The faint points represent clumps excluded from our study due to a high reduced-$\chi^2 > 4$. Meanwhile, the blue region indicates the disc fragmentation scales (λ_{2D}).

that are either more extended than a few kpc or smaller than 0.1 kpc. The same arguments presented in Section 2.4 to explain detection limits apply here. Clumps are challenging to model if they are much smaller than the PSF size or approach the disc size. The subsequent discussions on the mass–size relation will be taken up in Section 4.2.

3.4 Clump stellar mass function

The stellar mass function of clumps (cSMF) can also provide insights into their formation mechanisms (e.g. Elmegreen et al. 2006). Clumps formed through turbulent instabilities leading to cascading collapse (as discussed in Section 4.2) are expected to have a characteristic cSMF slope of $\alpha \approx -2.0 \pm 0.3$ (Elmegreen et al. 2006; Veltchev, Donkov & Klessen 2013; Chandar et al. 2014; Adamo et al. 2017; Zhou, Kroupa & Dib 2024). It is important to note, however, that these results are primarily based on low-z studies, where stellar clumps are limited to masses of $\sim 10^5 \, M_\odot$. This upper limit is due to the physical conditions at low-redshift. At $z > 1$, the scales would be much larger, as argued in Section 4.2, extending up to kpc-scale clumps with stellar masses $> 10^6 \, M_\odot$. None the less, they would still follow the same slope, given the underlying physics remains consistent (Dessauges-Zavadsky & Adamo 2018; Claeyssens et al. 2024).

It is important to note that the resolution limit may influence the fit, as the estimated mass may be a few times higher (Tamburello et al. 2017). However, the sensitivity limit has a more significant effect (Dessauges-Zavadsky & Adamo 2018). Therefore, limiting our study to clumps well within our completeness range is essential for accurately measuring the cSMF. We set a limit of $10^{8.7} \, M_\odot$, determined from the mass limit in Section 2.4. We find that the characteristic size of clumps with this mass would be ~ 0.4 kpc based
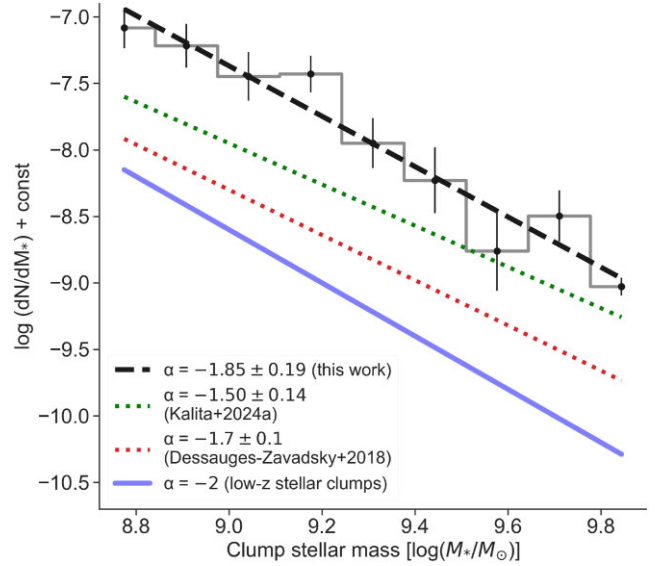

Figure 15. The clump stellar mass function in our sample is compared to previous studies (Dessauges-Zavadsky & Adamo 2018; Kalita et al. 2024a). This is further compared to the theoretical prediction for clumps formed from disc instabilities ($\alpha = -2$; Elmegreen et al. 2006). A constant has been added to the power law for a visual comparison of the slopes.

on equations (1). Thus, we exclude clumps that are unresolved in the detection image ($F150W$), without actually making it a criterion. This leaves 66 clumps in our sample. Using the number of clumps (N) and stellar mass ($M_\star$), we can fit our sample with the following equation:

$$\log(dN/dM_\star) = \alpha \log(M_\star) - \text{const}$$

We measure an $\alpha = -1.85 \pm 0.19$ (Fig. 15), which strongly agrees with the expected $\alpha \approx -2$. We also find this slope consistent with previous studies. Kalita et al. (2024a) report an $\alpha = -1.50 \pm 0.14$, which is slightly shallower than the expected value due to the lower resolution resulting from the use of images PSF-matched to that of $F444W$. Dessauges-Zavadsky & Adamo (2018) with an $\alpha = -1.7 \pm 0.1$, use clumps in lensed galaxies as well as results from an *HST*-based study (Elmegreen et al. 2013) at the higher mass end. Our measured value of α thus supports the conclusion that the massive stellar clumps in our study are likely part of the hierarchy of star-forming regions.

It is worth noting that we do not discuss the normalization of this relation. As highlighted by Dessauges-Zavadsky & Adamo (2018), normalization depends on detection thresholds and the star formation histories adopted, making direct comparisons between different studies challenging. This is why the aforementioned study does not refer to any specific value in their results. Although we find a similar normalization compared to Kalita et al. (2024a), we limit our discussion to the slope, which is relatively independent of these factors.

3.5 Residual spiral structures

A key feature of the analysis is the detection of underlying stellar structures in the form of residuals in the rest-frame near-IR images. These structures are not captured by the bulge + disc + clump models and thus appear as distinct entities in most galaxies in our study. We are not yet able to satisfactorily fit these features with
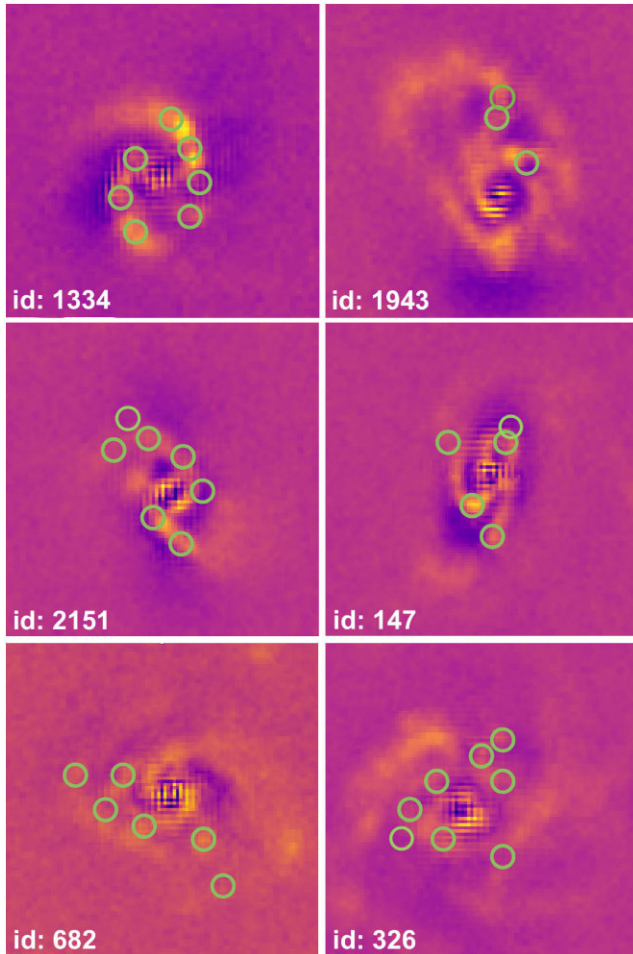
Figure 16. The location of all clumps (including detected clumps as well as those rejected due to high χ^2) on the rest-frame near-IR (*F444W*) residual images for 6/32 galaxies in our sample. The corresponding bulge + disc + clumps model has been subtracted to produce these images. We find > 70 per cent spatial association of clumps with residual spiral features in our study.

models and therefore rely on visual inspection. It should be noted that galaxies with clear signs of major mergers were already removed (Section 2.1). However, based on the residuals, we find that 5 out of 26 galaxies may be undergoing detectable levels of minor mergers, which could result in tidal features being misinterpreted as spiral arms.

Interestingly, 18 of the remaining clumpy galaxies in our sample show signs of spiral arms in the rest-frame near-IR residual images, while their optical image residuals reveal these features to varying degrees of prominence. When we examine the locations of the detected clumps in these galaxies (Fig. 16), we find an overwhelming association of over 70 per cent. The actual number could be higher since visual inspection can only establish associations if the residuals are detected at above 3σ. Furthermore, in some cases, spatial overlap may cause some flux from the residuals to leak into the clump model. This could dampen the residual flux near the clumps, making associations more challenging to identify.
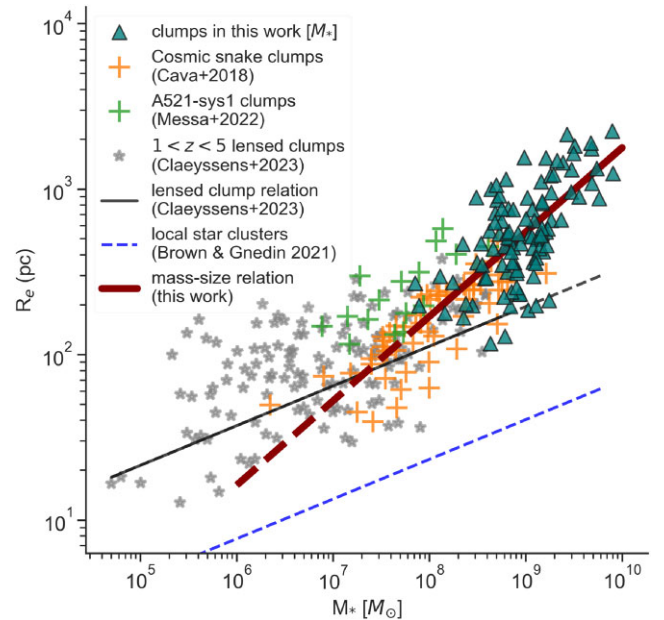
Figure 17. The comparison of the stellar clumps in this work to those in the lensed galaxies. Clumps in the Cosmic snake (Cava et al. 2018) and A521-sys1 (Messa et al. 2022) are provided with '+' symbols. The GMCs within these systems are later presented in Fig. 18. A larger set of clumps in 11 lensed galaxies at $1 < z < 5$ are shown with star symbols along with the corresponding scaling relation (Claeyssens et al. 2023). This relation also includes upper limits and clumps at $z > 5$, and thus does not precisely represent the distribution of clumps in the $1 < z < 5$ range presented. We also show the local star cluster relation (Brown & Gnedin 2021). In each case, solid lines indicate the region over which the respective relation is estimated, while dashed lines indicate extrapolation.

4 DISCUSSIONS

4.1 Multiscale nature of clumps

There has been a gap in mapping the size (and hence the mass) distribution of clumps between unlensed studies (investigating the massive end at $\gtrsim 1$ kpc, e.g. Genzel et al. 2006; Elmegreen et al. 2008; Guo et al. 2015, 2018) and lensed studies (targetting structures down to tens of parsecs, e.g. Jones et al. 2010; Livermore et al. 2012, 2015; Cava et al. 2018; Zick et al. 2020; Messa et al. 2022; Claeyssens et al. 2023, 2024). In this study, we find galaxy clumps in the range of $0.1 - 1$ kpc, bridging this gap and enabling more accurate size–mass measurements. This has been achieved primarily due to the high-angular resolution of *JWST*/NIRCam images, which cover the rest-frame optical wavelengths, combined with the depth of the COSMOS-Web data.

When placed within the same mass–size parameter space, we find that the lensed clumps from 13 galaxies within $1 < z < 5$, observed over various magnifications, extend the distribution of our sample down to $\sim 10^6$ M$_\odot$ (Fig. 17). With overlap only at ~ 100 pc, the absence of smaller clumps in our study is due to completeness limits (Fig. 7). Our sample also overlaps with other lensed systems in Jones et al. (2010) and Livermore et al. (2012, 2015), which show similar clump sizes and stellar mass ranges of $\sim 0.06 - 1$ kpc and 10^{8-9} M$_\odot$. Comparisons to the (largest yet) compilation of clumps in lensed galaxies in Claeyssens et al. (2023, 2024) also highlights the clumps in our sample overlaps with the massive end of the full range of clump masses observed in these studies.

We conclude that resolution is indeed critical in determining the detectable clump distribution. Higher resolution would likely reveal smaller clumps in both size and mass. However, this raises the question of the relevance of massive clumps. Are they merely blended star clusters observed as single objects due to resolution limits? At $\lesssim 10$ pc scales, achievable using lensing at $z > 1$, one approaches the size of star clusters (Vanzella et al. 2017a, b, 2022a, b; Welch et al. 2022; Adamo et al. 2024; Mowla et al. 2024; Messa et al. 2024a). The compilation work in Claeyssens et al. (2023) suggests a similar clump size–stellar mass relation $[r_e = 12.3 \pm 10.0 \times (\frac{M_\star}{10^4\,M_\odot})^{0.24\pm0.10}]$ to that expected in local star clusters $[r_e = 2.55 \times (\frac{M_\star}{10^4\,M_\odot})^{0.24}$; Brown & Gnedin 2021, also shown in Fig. 17].

However, structures at larger scales (> 100 pc) cannot be a simple extrapolation of this relation, as it would suggest an increase in mass density with size. The similarity of the cSMF to that of hierarchical star-forming regions at low-z (Section 3.4) indicates that the clump structure likely has a hierarchical nature (Dessauges-Zavadsky & Adamo 2018). The $r_e \propto M_\star^{0.52\pm0.07}$ relation we measure in Section 3.3 supports this scenario since it leads to a decreasing mass density with size. Thus, similar to low-z, clumps would then likely be part of hierarchical star-forming structures that are regulated by cascading turbulent motions and self-gravity (Elmegreen & Efremov 1996; Elmegreen & Scalo 2004; Bergin & Tafalla 2007; Grasha et al. 2017; Rodríguez, Baume & Feinstein 2020). The source of such turbulence, which influences clump formation, is debated; possible contributors include stellar feedback, gravitational energy from accreting gas, gravitational torques, and clump collisions (Immeli et al. 2004; Khochfar & Silk 2009; Ceverino, Dekel & Bournaud 2010; Elmegreen & Burkert 2010; Krumholz & Burkert 2010; Murray et al. 2010).

This hierarchical nature of clumps has been suggested by both simulations and direct observations. Several simulation studies (Ceverino et al. 2012; Behrendt, Burkert & Schartmann 2016; Behrendt, Schartmann & Burkert 2019; Faure et al. 2021) find that clumps exhibit significant sub-structures. Observations in some cases, where different lensing magnifications reveal clumps with hierarchical structures, also support this idea (Fisher et al. 2017; Cava et al. 2018; Messa et al. 2019, 2022). Therefore, if the clumps in our sample were observed with higher resolution, one would likely detect the smaller structures within them (sub-clumps or possibly star clusters).

4.2 Instability-driven clump formation

It is important to understand the physics behind the formation of these multiscale clumps. There are two primary formation modes. '*In situ*' clumps arise as a result of disc instabilities with ages from tens (short-lived) to a few hundred Myr (long-lived). Meanwhile, *ex situ* clumps refer to infalling stellar bodies that form outside the galaxy (Förster Schreiber et al. 2011; Wuyts et al. 2012; Zanella et al. 2015). The latter are expected to have characteristically higher stellar ages (Mandelker et al. 2017), with the assumption that these clumps do not get tidally disrupted by the galaxy potential well. These are found to be relatively rare (Bournaud 2016), but could contribute to the UV/optically faint near-IR detected clumps in Kalita et al. (2024a).

The age estimations from our analysis can only constrain an upper limit for the clumps at ~ 700 Myr on average. This is not sufficient to distinguish between short-lived and long-lived *in situ* clumps. However, with the expected ages of *ex situ* clumps being $\gtrsim 1$ Gyr (Mandelker et al. 2017), we do not expect them to be contributing substantially to our sample. This is likely a result of

the rest-frame optical selection and a requirement for the SED to be well fit with a constant star formation history model (Section 3.2 and Appendix C). The small contribution of the *ex situ* clumps maybe expected to make up the most massive end of the clump mass–size relation (Fig. 14). However, visual inspection alone is insufficient to accurately determine which galaxies in our sample are undergoing minor-mergers. A robust classification would only be possible with resolved kinematic data.

Within the instability-driven framework, clumps are believed to result from disc fragmentation (Elmegreen et al. 2008; Genzel et al. 2011). This fragmentation is governed by the Toomre instability criterion, defined as a function of disc surface mass density (Σ), epicyclic frequency (κ), and velocity dispersion (σ):

$$Q = \frac{\sigma \kappa}{\pi G \Sigma} \le 1.$$

Based on this criterion, the Toomre length (λ_T) can be defined as the largest scale over which a disc can fragment due to self-gravity. As described in Genzel et al. (2023), this length can be approximated by:

$$\lambda_T = \frac{\pi^2 G \Sigma}{v_{\rm rot}/r_{\rm disc}} \sim f_g\, r_{\rm disc},$$

where $v_{\rm rot}$ is the disc rotational velocity, $r_{\rm disc}$ is the disc radius, and f_g is the gas fraction. Using the values of f_g for our sample and substituting r_{90} for $r_{\rm disc}$, we find $\lambda_T \sim 1 - 5$ kpc. This indicates the largest scales below which fragmentation can occur, which may go down to the classical Jeans length. The caveat being that the analytic Toomre theory requires $Q \approx 1$.

Another model for instability-driven fragmentation is provided by Meidt (2022), where they adopt a 3D perspective of the galaxy disc. In this new framework, the most unstable 2D wavelength is defined as λ_{2D}. This is the scale over which fragmentation occurs under the condition that the Toomre parameter:

$$Q = \left(\frac{\lambda_{2D}}{2\,\lambda_T}\right)^{1/2} \le 1.$$

For $Q \gtrsim 1$, λ_{2D} exceeds λ_T, indicating a stable disc, as rotation prevents the growth of perturbations on scales $\ge \lambda_T$. For $Q < 1$, λ_{2D} can fall below λ_T. Assuming the galaxies in our sample are unstable with $Q < 1$, we approximate this parameter using the relation from Meidt (2022):

$$\lambda_{2D} = \frac{2\sigma^2}{G\Sigma},$$

where Σ is the total mass surface density of the galaxy discs.[13] The parameter σ is the velocity dispersion, assumed to approximate the ionized gas velocity dispersion. We use empirical values of $\sigma = 40 \pm 20$ km s^{-1} for $z \sim 1.5$ from Übler et al. (2019). The estimated λ_{2D} ranges from $\sim 0.2 - 5$ kpc, which is broadly similar to λ_T, but with a slightly lower limit.

Regarding the lower limit near the Jeans length (λ_J), most studies ignore disc thickness while measuring it (e.g. Hopkins et al. 2012; Livermore et al. 2012, 2015). However, considering the 3D nature of the discs, Meidt (2022) estimates λ_J, which is also related to λ_{2D}:

$$\lambda_J = \frac{\sigma \pi^{1/2}}{(G\rho)^{1/2}} = \lambda_{2D}\frac{f_g^{1/2}}{\pi},$$

where f_g is the disc gas fraction and ρ is the interstellar medium (ISM) density. As discussed in Meidt et al. (2023), this can be

---

[13]Estimated using $0.9\times$ the stellar + gas mass and $\pi \times r_{90}^2$.

considered the lower bound on 3D fragmentation at the mid-plane of rotating discs. We estimate λ_J to be $\sim 10 - 500$ pc. All clumps across various scales (including lensed clumps from the literature) can be hence be approximately regarded as instabilities spanning from λ_T ($\sim \lambda_{2D}$) down to $\sim \lambda_J$. The hierarchy of the clumps discussed in Section 4.1 therefore likely exists within this range. Meanwhile, the size limit of detected clumps would then depend on the resolution limit of the observations.

4.3 GMCs and clumps

An integral part of the hierarchical and self-similar distribution of star-forming structures in the ISM, which we conclude the clumps to form a part of, are the gas clouds. We therefore explore the possibility of molecular gas cloud progenitors of the massive clumps in our study. This is especially interesting since the scaling $r_e \propto M_\star^{0.52\pm0.07}$ for the clumps mirrors that of GMCs (size $\sim$ mass$^{0.5}$; Heyer & Dame 2015, for a review). GMCs also exhibit a hierarchical structure shaped by turbulence, gravitational interactions, and magnetic fields, while also merging to form larger cloud complexes. However, a direct correlation is challenging to establish since the clumps we detect are too large to form at the cores of virialized GMCs as observed in the local Universe. Simulations also suggest that gas-rich galaxies featuring massive clumps would host GMCs of 10^{5-7} M$_\odot$, which are expected to be destroyed within $10 - 30$ Myr by stellar feedback (Ceverino et al. 2014; Perret et al. 2014). This time-scale is similar to the lifetimes of GMCs in the local Universe (Kawamura et al. 2009; Kruijssen et al. 2019; Chevance et al. 2020; Kim, Ostriker & Filippova 2021).

However, instabilities in gas discs should result in clumpy molecular gas morphologies (Vázquez-Semadeni et al. 2019). Detecting such GMCs at $z \gtrsim 1$ is extremely challenging, and they have only recently been observed in a few sources (Dessauges-Zavadsky et al. 2019, 2023). We provide a qualitative comparison of these GMCs with our clump sample in Fig. 18. The distinct (but proportional) differences are also evident in the stellar clumps within these systems that host the GMCs (comparing to Fig. 17). These stellar clumps are often spatially offset from the GMCs (Dessauges-Zavadsky et al. 2019; Messa et al. 2022). Nevertheless, the mass of these GMCs could represent the parent gas clouds for clumps similar to the less massive ones in these systems. It is also important to note that, at low z, a direct spatial association between GMCs and clumps has been observed only at scales $\gtrsim 0.5$ kpc (due to possible dissipation of GMCs by stellar feedback; Pan et al. 2022).

We compared these stellar clumps to our sample in Section 4.1. However, it is worth noting that the two systems we refer to have gas fractions of 14–25 per cent, while our sample has fractions of $\gtrsim 40$ per cent, with gas reservoirs larger by more than an order of magnitude. Consequently, the associated turbulent dispersion would result not only in larger clumps (Genzel et al. 2011; Livermore et al. 2015) but also in larger GMCs (Larson 1981) in our sample. Thus, a direct one-to-one comparison would not be appropriate. More extensive GMC statistics at $z \gtrsim 1$ are needed to draw a conclusion and establish an observational link between these and massive clumps.

4.4 Clumps within spirals

The appearance of spiral arms in galaxies at $z \lesssim 2.5$ (Margalef-Bentabol et al. 2022) is particularly intriguing in relation to the star-forming clumps within these systems. These 'clumpy spirals' likely represent a significant phase in the evolution of massive disc
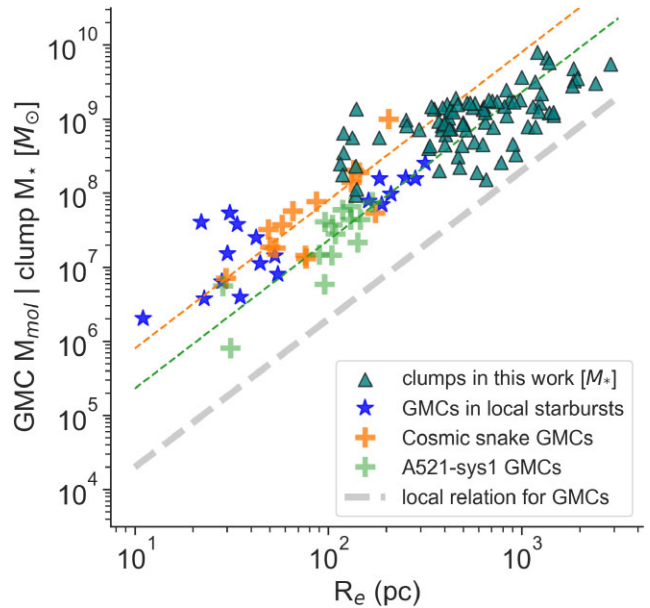

Figure 18. The comparison of the stellar clumps in this work to GMCs. These compiled datapoints have been taken from the work that contributes the values for the A521-sys1 GMCs (Dessauges-Zavadsky et al. 2023). The other values included here are from the Cosmic snake (Dessauges-Zavadsky et al. 2019), and GMCs in local starbursts (Wei, Keto & Ho 2012; Leroy et al. 2015).

galaxies, marking the transition from the high-z clumpy phase to the low-z spiral phase (Elmegreen & Elmegreen 2014). However, these two phases may not be mutually exclusive. Spiral arms typically form due to a low Toomre parameter ($Q < 1$) in the stellar component. Low values of Q_{star} result in prominent grand design spirals, while higher values of Q_{star} produce fainter 'flocculent' spirals with patchy arms (Elmegreen & Elmegreen 1987). Meanwhile, the presence of massive clumps suggests low values of both Q_{star} and Q_{gas}.

Bournaud & Elmegreen (2009) suggests that hosts of massive clumps within spirals are likely massive galaxies with high stellar masses, which would have thick discs and even spheroids, enhancing the likelihood of spiral arm formation. Thus, it is not surprising that our sample of massive clumpy galaxies ($> 10^{10.5}$ M$_\odot$) predominantly features spiral structures. However, the relative prevalence of spirals and clumps in our sample may provide further insights into the stability of these galaxies. We will explore this in follow-up papers (Kalita et al. submitted to ApJL; Kalita et al., in preparation).

Finally, some regions in the rest-frame near-IR residuals may be considered clumps that remain undetected in the $F150W$ band due to high levels of dust obscuration. A near-IR selection, as in Kalita et al. (2024a), would have detected them. This further highlights the intrinsic link between clumps and extended stellar structures, with the distinction varying across wavelengths.

5 CONCLUSIONS

The details of clump formation are not fully understood due to limitations in-depth and resolution, which typically allow the detection of only kpc-scale clumps in large statistical samples (e.g. Wuyts et al. 2012; Guo et al. 2015, 2018). In contrast, lensed studies suggest that clumps have smaller characteristic sub-kpc sizes (e.g. Jones et al. 2010; Livermore et al. 2012; Cava et al. 2018). Studies also indicate that the lack of high-resolution data (~ 100 pc) can lead

to an overestimation of physical properties (Tamburello et al. 2015; Fisher et al. 2017; Huertas-Company et al. 2020). Proper clump characterization is therefore crucial for understanding how disc instabilities lead to their formation (Elmegreen et al. 2009; Genzel et al. 2011). *JWST* is well positioned to measure clump properties with high-resolution multiwavelength data. At $z \sim 1.5$, this coverage translates to the rest-frame optical- to near-IR. Moreover, for the shortest wavelengths, structures like clumps can be detected down to physical scales of ~ 0.1 kpc.

In this work, we use data from *JWST*/NIRCam (four bands) to construct bulge, disc, and clump models for 32 galaxies with spectroscopic redshift ~ 1.5. We also use the bulge and disc model to decompose ALMA Band-7 data. The galaxies have stellar masses above $10^{10.6}$ M$_\odot$ and lie on the star-forming main-sequence. Using the rest-frame optical *F150W* filter, we detect and model star-forming clumps in 26 of these galaxies. The key conclusions of this paper are:

(i) The star-forming clumps have a range of stellar masses ($\sim 10^{8.1-9.5}$ M$_\odot$) and sizes ($r_e \sim 0.1 - 1$ kpc). We also assess the detection limits of our method as a function of *F150W* flux (and thus stellar mass) and size. The final sample of clumps is within the 90 per cent completeness regime. All clumps are star-forming with high $\Sigma_{SFR} = 10^{-2} - 10^2$ M$_\odot$ yr^{-1} kpc^{-2}. Each clump shows an increased sSFR compared to its host but lies within the scatter of the star-forming main-sequence for its respective stellar mass.

(ii) We find a strong correlation between the stellar mass and size of the clumps, from which we derive an empirical stellar mass–size relation. The extension of this relation aligns with smaller clumps found in lensed studies, which may also include star clusters. Thus, we conclude that the clumps are part of a hierarchical structure, similar to that observed in star-forming regions in the local Universe.

(iii) We measure a stellar mass function slope of -1.85 ± 0.19 for the clumps, in remarkable agreement with the hierarchical star-forming regions ($\alpha \approx -2$) observed in local galaxies. This also suggests that these structures are likely shaped by multiscale turbulent motions and self-gravity.

(iv) We conclude that the clumps detected in our study along with those which maybe below our detection limit (< 100 pc) likely cover the range of scales bound by the Toomre length ($\sim$ a few kpc) and the Jeans length ($\sim$ tens to a few hundred pc).

(v) After subtracting the bulge, disc, and clump components, we clearly observe spiral features in the rest-frame near-IR residual images. There is an association of > 70 per cent between the clumps and the spiral features. We require to properly characterize these features to help us understand the evolution of the dynamical stability of massive stellar discs at high z.

In conclusion, we find that the improved imaging using *JWST*/NIRCam and modelling capabilities of this study allow us to properly characterize clumps in the most massive star-forming galaxies at $z \sim 1.5$. The observational divide between lensed and unlensed studies is reduced, thereby distributing their properties over a wide range of characteristic mass and size. We find that the entire clump population can be explained by instability-driven coherent collapse and resulting star formation. The limitations of using only imaging data and, consequently, anticipating the dynamics involved can be overcome by obtaining high-resolution spectroscopic data. This will provide the final piece of this coherent picture of galaxy clumps.

DATA AVAILABILITY

All *JWST* and *HST* data products are available via the Mikulski Archive for Space Telescopes (https://mast.stsci.edu). The ALMA data are available on the ALMA Science Archive at https://almascience.eso.org/asax/.

REFERENCES

Abraham R. G., van den Bergh S., Glazebrook K., Ellis R. S., Santiago B. X., Surma P., Griffiths R. E., 1996, ApJS, 107, 1

Adamo A., Östlin G., Bastian N., Zackrisson E., Livermore R. C., Guaita L., 2013, ApJ, 766, 105

Adamo A. et al., 2017, ApJ, 841, 131

Adamo A. et al., 2024, Nature, 632, 513

Astropy Collaboration, 2022, ApJ, 935, 167

Behrendt M., Burkert A., Schartmann M., 2016, ApJ, 819, L2

Behrendt M., Schartmann M., Burkert A., 2019, MNRAS, 488, 306

Bergin E. A., Tafalla M., 2007, ARA&A, 45, 339

Bertin E., 2011, in Evans I. N., Accomazzi A., Mink D. J., Rots A. H., eds, ASP Conf. Ser. Vol. 442, Astronomical Data Analysis Software and Systems XX. Astron. Soc. Pac., San Francisco, p. 435

Béthermin M. et al., 2015, A&A, 573, A113

Bigiel F., Leroy A., Walter F., Brinks E., de Blok W. J. G., Madore B., Thornley M. D., 2008, AJ, 136, 2846

Birrer S., Amara A., 2018, Phys. Dark Universe, 22, 189

Birrer S. et al., 2021, J. Open Source Softw., 6, 3283

Boquien M., Burgarella D., Roehlly Y., Buat V., Ciesla L., Corre D., Inoue A. K., Salas H., 2019, A&A, 622, A103

Bournaud F., 2016, in Laurikainen E., Peletier R., Gadotti D., eds, Astrophysics and Space Science Library Vol. 418, Galactic Bulges. Springer International Publishing, Switzerland, p.355

Bournaud F., Elmegreen B. G., 2009, ApJ, 694, L158

Brown G., Gnedin O. Y., 2021, MNRAS, 508, 5935

Bruzual G., Charlot S., 2003, MNRAS, 344, 1000

Buck T., Macciò A. V., Obreja A., Dutton A. A., Domínguez-Tenreiro R., Granato G. L., 2017, MNRAS, 468, 3628

Calzetti D., Armus L., Bohlin R. C., Kinney A. L., Koornneef J., Storchi-Bergmann T., 2000, ApJ, 533, 682

Casey C. M. et al., 2023, ApJ, 954, 31

Cava A., Schaerer D., Richard J., Pérez-González P. G., Dessauges-Zavadsky M., Mayer L., Tamburello V., 2018, Nat. Astron., 2, 76

Ceverino D., Dekel A., Bournaud F., 2010, MNRAS, 404, 2151

Ceverino D., Dekel A., Mandelker N., Bournaud F., Burkert A., Genzel R., Primack J., 2012, MNRAS, 420, 3490

Ceverino D., Klypin A., Klimek E. S., Trujillo-Gomez S., Churchill C. W., Primack J., Dekel A., 2014, MNRAS, 442, 1545

Chabrier G., 2003, PASP, 115, 763

Chandar R., Whitmore B. C., Calzetti D., O'Connell R., 2014, ApJ, 787, 17

Chevance M. et al., 2020, MNRAS, 493, 2872

Claeyssens A., Adamo A., Richard J., Mahler G., Messa M., Dessauges-Zavadsky M., 2023, MNRAS, 520, 2180

Claeyssens A., Adamo A., Messa M., Dessauges-Zavadsky M., Richard J., Kramarenko I., Matthee J., Naidu R. P., 2024, preprint (arXiv:2410.10974)

Cook D. O., Dale D. A., Lee J. C., Thilker D., Calzetti D., Kennicutt R. C., 2016, MNRAS, 462, 3766

Cowie L. L., Hu E. M., Songaila A., 1995, AJ, 110, 1576

Daddi E., Dannerbauer H., Elbaz D., Dickinson M., Morrison G., Stern D., Ravindranath S., 2008, ApJ, 673, L21

Daddi E. et al., 2010, ApJ, 713, 686

Dekel A., Birnboim Y., 2006, MNRAS, 368, 2

Dessauges-Zavadsky M., Adamo A., 2018, MNRAS, 479, L118

Dessauges-Zavadsky M., Schaerer D., Cava A., Mayer L., Tamburello V., 2017, ApJ, 836, L22

Dessauges-Zavadsky M. et al., 2019, Nat. Astron., 3, 1115

Dessauges-Zavadsky M. et al., 2023, MNRAS, 519, 6222

Ding X., Silverman J. D., Onoue M., 2022, ApJ, 939, L28

Draine B. T., Li A., 2007, ApJ, 657, 810

Elbaz D. et al., 2018, A&A, 616, A110

Elmegreen B. G., Burkert A., 2010, ApJ, 712, 294

Elmegreen B. G., Efremov Y. N., 1996, ApJ, 466, 802

Elmegreen D. M., Elmegreen B. G., 1987, ApJ, 314, 3

Elmegreen B. G., Elmegreen D. M., 2005, ApJ, 627, 632

Elmegreen D. M., Elmegreen B. G., 2014, ApJ, 781, 11

Elmegreen B. G., Scalo J., 2004, ARA&A, 42, 211

Elmegreen B. G., Elmegreen D. M., Chandar R., Whitmore B., Regan M., 2006, ApJ, 644, 879

Elmegreen D. M., Elmegreen B. G., Ravindranath S., Coe D. A., 2007, ApJ, 658, 763

Elmegreen B. G., Bournaud F., Elmegreen D. M., 2008, ApJ, 688, 67

Elmegreen D. M., Elmegreen B. G., Marcus M. T., Shahinyan K., Yau A., Petersen M., 2009, ApJ, 701, 306

Elmegreen B. G., Elmegreen D. M., Sánchez Almeida J., Muñoz-Tuñón C., Dewberry J., Putko J., Teich Y., Popinchalk M., 2013, ApJ, 774, 86

Epinat B. et al., 2012, A&A, 539, A92

Faure B., Bournaud F., Fensch J., Daddi E., Behrendt M., Burkert A., Richard J., 2021, MNRAS, 502, 4641

Fisher D. B. et al., 2017, MNRAS, 464, 491

Förster Schreiber N. M. et al., 2011, ApJ, 739, 45

Fujimoto S. et al., 2024, preprint (arXiv:2402.18543)

Geach J. E., Smail I., Moran S. M., MacArthur L. A., Lagos C. d. P., Edge A. C., 2011, ApJ, 730, L19

Genzel R. et al., 2006, Nature, 442, 786

Genzel R. et al., 2011, ApJ, 733, 101

Genzel R. et al., 2023, ApJ, 957, 48

Gómez-Guijarro C. et al., 2018, ApJ, 856, 121

Grasha K. et al., 2017, ApJ, 842, 25

Guo Y. et al., 2015, ApJ, 800, 39

Guo Y. et al., 2018, ApJ, 853, 108

Heyer M., Dame T. M., 2015, ARA&A, 53, 583

Hinojosa-Goñi R., Muñoz-Tuñón C., Méndez-Abreu J., 2016, A&A, 592, A122

Hodge J. A. et al., 2024, preprint (arXiv:2407.15846)

Hopkins P. F., Kereš D., Murray N., Quataert E., Hernquist L., 2012, MNRAS, 427, 968

Hopkins P. F., Kereš D., Oñorbe J., Faucher-Giguère C.-A., Quataert E., Murray N., Bullock J. S., 2014, MNRAS, 445, 581

Hopkins P. F. et al., 2023, MNRAS, 525, 2241

Huertas-Company M. et al., 2020, MNRAS, 499, 814

Immeli A., Samland M., Gerhard O., Westera P., 2004, A&A, 413, 547

Johnson T. L. et al., 2017, ApJ, 843, L21

Jones T. A., Swinbank A. M., Ellis R. S., Richard J., Stark D. P., 2010, MNRAS, 404, 1247

Kalita B. S. et al., 2022, A&A, 666, A44

Kalita B. S., Silverman J. D., Daddi E., Mercier W., Ho L. C., Ding X., 2024a, preprint (arXiv:2402.02679)

Kalita B. S., Silverman J. D., Daddi E., Bottrell C., Ho L. C., Ding X., Yang L., 2024b, ApJ, 960, 25

Kashino D. et al., 2013, ApJ, 777, L8

Kashino D. et al., 2019, ApJS, 241, 10

Kawamura A. et al., 2009, ApJS, 184, 1

Kennedy J., Eberhart R., 1995, in Proc. ICNN'95 – International Conference on Neural Networks, Vol. 4. IEEE, p. 1942

Kennicutt Robert C.J., De Los Reyes M. A. C., 2021, ApJ, 908, 61

Khochfar S., Silk J., 2009, ApJ, 700, L21

Kim J.-G., Ostriker E. C., Filippova N., 2021, ApJ, 911, 128

Koekemoer A. M. et al., 2007, ApJS, 172, 196

Kruijssen J. M. D., Pfeffer J. L., Reina-Campos M., Crain R. A., Bastian N., 2019, MNRAS, 486, 3180

Krumholz M., Burkert A., 2010, ApJ, 724, 895

Krumholz M. R., Dekel A., 2010, MNRAS, 406, 112

Larson R. B., 1981, MNRAS, 194, 809

Larson K. L. et al., 2020, ApJ, 888, 92

Leitherer C., Li I. H., Calzetti D., Heckman T. M., 2002, ApJS, 140, 303

Leroy A. K., Walter F., Brinks E., Bigiel F., de Blok W. J. G., Madore B., Thornley M. D., 2008, AJ, 136, 2782

Leroy A. K. et al., 2015, ApJ, 814, 83

Liu Z. et al., 2024, ApJ, 968, 15

Livermore R. C. et al., 2012, MNRAS, 427, 688

Livermore R. C. et al., 2015, MNRAS, 450, 1812

Magdis G. E. et al., 2012, ApJ, 760, 6

Mandelker N., Dekel A., Ceverino D., Tweed D., Moody C. E., Primack J., 2014, MNRAS, 443, 3675

Mandelker N., Dekel A., Ceverino D., DeGraf C., Guo Y., Primack J., 2017, MNRAS, 464, 635

Margalef-Bentabol B., Conselice C. J., Haeussler B., Casteels K., Lintott C., Masters K., Simmons B., 2022, MNRAS, 511, 1502

Martig M., Bournaud F., Teyssier R., Dekel A., 2009, ApJ, 707, 250

McKee C. F., Ostriker E. C., 2007, ARA&A, 45, 565

Mehta V. et al., 2021, ApJ, 912, 49

Meidt S. E., 2022, ApJ, 937, 88

Meidt S. E. et al., 2023, ApJ, 944, L18

Messa M., Adamo A., Östlin G., Melinder J., Hayes M., Bridge J. S., Cannon J., 2019, MNRAS, 487, 4238

Messa M., Dessauges-Zavadsky M., Richard J., Adamo A., Nagy D., Combes F., Mayer L., Ebeling H., 2022, MNRAS, 516, 2420

Messa M. et al., 2024a, preprint (arXiv:2407.20331)

Messa M., Dessauges-Zavadsky M., Adamo A., Richard J., Claeyssens A., 2024b, MNRAS, 529, 2162

Meštrić U. et al., 2022, MNRAS, 516, 3532

Mowla L. et al., 2024, preprint (arXiv:2402.08696)

Murray N., Quataert E., Thompson T. A., 2010, ApJ, 709, 191

Oklopčić A., Hopkins P. F., Feldmann R., Kereš D., Faucher-Giguère C.-A., Murray N., 2017, MNRAS, 465, 952

Pan H.-A. et al., 2022, ApJ, 927, 9

Perret V., Renaud F., Epinat B., Amram P., Bournaud F., Contini T., Teyssier R., Lambert J. C., 2014, A&A, 562, A1

Puglisi A. et al., 2019, ApJ, 877, L23

Rahman N. et al., 2012, ApJ, 745, 183

Reina-Campos M., Kruijssen J. M. D., 2017, MNRAS, 469, 1282

Rodríguez M. J., Baume G., Feinstein C., 2020, A&A, 644, A101

Rujopakarn W. et al., 2023, ApJ, 948, L8

Schinnerer E., Leroy A. K., 2024, ARA&A, 62, 369

Schreiber C. et al., 2015, A&A, 575, A74

Scoville N. et al., 2007, ApJS, 172, 1

Sharda P., Federrath C., da Cunha E., Swinbank A. M., Dye S., 2018, MNRAS, 477, 4380

Sheth K. et al., 2010, PASP, 122, 1397

Shibuya T., Ouchi M., Kubo M., Harikane Y., 2016, ApJ, 821, 72

Silverman J. D. et al., 2015, ApJS, 220, 12

Soto E. et al., 2017, ApJ, 837, 6

Spergel D. N., 2010, ApJS, 191, 58

Tacconi L. J. et al., 2010, Nature, 463, 781

Tacconi L. J. et al., 2013, ApJ, 768, 74

Tamburello V., Mayer L., Shen S., Wadsley J., 2015, MNRAS, 453, 2490

Tamburello V., Rahmati A., Mayer L., Cava A., Dessauges-Zavadsky M., Schaerer D., 2017, MNRAS, 468, 4792

Tan Q.-H. et al., 2024a, Nature, 636, 69

Tan Q.-H. et al., 2024b, A&A, 684, A23

Übler H. et al., 2019, ApJ, 880, 48

van den Bergh S., Abraham R. G., Ellis R. S., Tanvir N. R., Santiago B. X., Glazebrook K. G., 1996, AJ, 112, 359

Vanzella E. et al., 2017a, MNRAS, 467, 4304

Vanzella E. et al., 2017b, ApJ, 842, 47

Vanzella E. et al., 2022a, A&A, 659, A2

Vanzella E. et al., 2022b, ApJ, 940, L53

Vázquez-Semadeni E., Palau A., Ballesteros-Paredes J., Gómez G. C., Zamora-Avilés M., 2019, MNRAS, 490, 3061

Veltchev T. V., Donkov S., Klessen R. S., 2013, MNRAS, 432, 3495

Weaver J. R. et al., 2022, ApJS, 258, 11

Wei L. H., Keto E., Ho L. C., 2012, ApJ, 750, 136

Welch B. et al., 2022, ApJ, 940, L1

Wuyts S. et al., 2012, ApJ, 753, 114

Zanella A. et al., 2015, Nature, 521, 54

Zhou J.-w., Kroupa P., Dib S., 2024, A&A, 688, L19

Zick T. O., Weisz D. R., Ribeiro B., Kriek M. T., Johnson B. D., Ma X., Bouwens R., 2020, MNRAS, 493, 5653

APPENDIX A: SPATIAL DECONSTRUCTION: *JWST*

Here, we detail the spatial 'deconstruction' of *JWST* images of galaxies into their constituent components: bulge, disc, and clumps (Fig. A1). This was briefly discussed in Section 2.2. For this method, we use the rest-frame near-IR *F444W* image to optimize the bulge + disc model and the rest-frame optical *F150W* image to optimize the star-forming clumps. The fitting is performed using the PYTHON based package GALIGHT[14] (Ding, Silverman & Onoue 2022), which implements the forward-modelling galaxy image fitting tool LENSTRONOMY[15] (Birrer & Amara 2018; Birrer et al. 2021). This approach provides access to the full posterior distribution of each fitted parameter. The fitting is then optimized using the particle swarm optimizer (PSO; Kennedy & Eberhart 1995). All errors are estimated by artificially adding structures of similar sizes and fluxes

---

[14]https://github.com/dartoon/galight

[15]https://github.com/lenstronomy/lenstronomy

and remeasuring them (Tang et al., in preparation). The PSFs are created using the software PSFEX (Bertin 2011) on the full COSMOS-Web mosaics (Casey et al. 2023).

A1 Bulge and disc in *F444W*

To fit the *F444W* image, we start with a single Sérsic fit, allowing all spatial parameters to vary freely, as a reference. Given that the galaxies in our sample lie on the main-sequence and exhibit centrally concentrated star formation (Kalita et al., in preparation), we use a fixed Sérsic index ($n = 2$) for the bulge and $n = 1$ for the disc, assuming a pseudo-bulge rather than a classical bulge ($n = 4$). However, we find that our results remain unchanged even if $n = 4$ is used. In each of the 32 galaxies in our final sample, the bulge and disc model provides a better fit than the single Sérsic fit ($\mathrm{BIC_{bulge+disc}} < \mathrm{BIC_{single\_sersic}}$). With the final bulge + disc model, we fix all shape parameters and allow only the flux of the bulge to vary independently when fitting the rest-frame optical (*F150W*) image. As discussed in the main text, we find very high BIC values and significant residual flux, indicating the need for additional models to account for the clumpy sub-structures, which will be addressed in the next section.

A2 Adding the clumps in *F150W*

The clumps with high levels of Σ_{SFR} (Section 3.2), are most prominent in the rest-frame optical (Fig. 6). We therefore use the *F150W* image to model the clump profiles. We start with the widely used detection method (most recently in Kalita et al. 2024b), where a contrast map is created using the difference between the original image and a smoothed version (with a Gaussian kernel of $\sigma = 3$ pixels). Using a broader kernel for smoothing would prevent detection of the smallest sources, limiting the resolution of the *F150W*. Any smaller smoothing will approach the PSF, decreasing the flux in the contrast image and making clump detection more challenging.

We then apply σ-thresholding to detect clumps in the residual image, estimating σ using the *sigma_clipped_stats* feature in the ASTROPY package (Astropy Collaboration 2022). Starting with a depth of 10σ to identify clump locations, we progressively lower the threshold to 3σ. Any detection with < 5 pixels will not be considered. At each step, we use the bulge + disc model from *F444W* and add Gaussian profiles at the clump locations (initialized with sizes equal to 1.5 times the PSF), allowing the clump flux and size to vary. The shape of the bulge + disc model is fixed, but the flux of each component is allowed to change. We estimate the BIC at each step to assess the goodness of fit given the model's added complexity. In each case, the best BIC is reached at either 3 or 4σ. At the end of this process, we obtain a final bulge + disc + clump model, which we use with fixed shapes to measure the flux of each component in each filter.
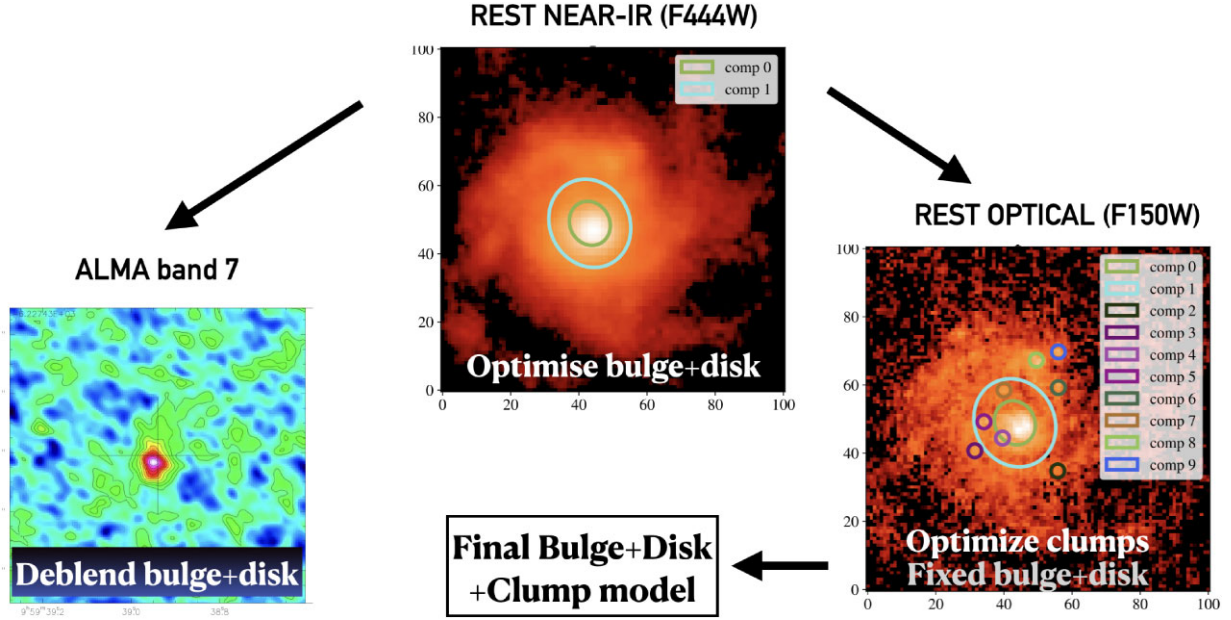
Figure A1. A flowchart describing the process of galaxy deconstruction used in this work. We start with optimizing the bulge and disc model in *F*444*W*. This is used along with clumps in the *F*150*W* image to finally get a bulge + disc + clump model. The ellipses indicate the *initial* guesses for each component. The same bulge and disc model is used to deblend the flux in the ALMA Band-7 image to divide to net flux into a bulge and disc component.
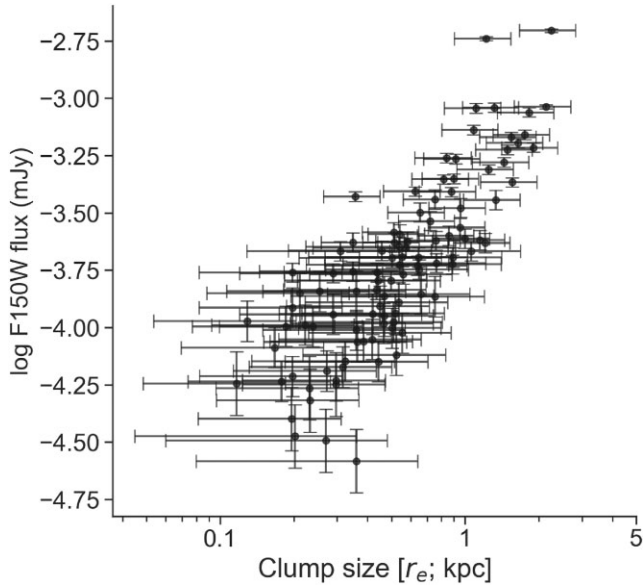

Figure A2. The clump size (r_e) versus the *F*150*W* flux for the clumps in our sample.

APPENDIX B: SPATIAL DECONSTRUCTION: ALMA BAND-7

For the ALMA Band-7 flux measurements, we use only the bulge and disc model, as the resolution and S/N are insufficient to measure the clumps. We assume that the 870 μm flux can be decomposed into bulge and disc components, based on recent observational evidence that the sub-mm flux follows the stellar mass maps traced by the rest-frame near-IR.

For the fitting, we use the UV-plane rather than the image plane, which has been shown to perform better due to the absence of

mathematical approximations involved in deconvolution and imaging (Tan et al. 2024b). The software used is GILDAS,[16] which has been widely employed for complex morphological modelling of ALMA images in several studies (e.g. Kalita et al. 2022; Tan et al. 2024b).

Since the Sérsic profile used in the bulge + disc model cannot be directly converted to the UV-plane due to its Fourier transform not being analytically expressible, we instead use the Spergel profile (Spergel 2010). This profile correlates well with the Sérsic profile, allowing us to translate the bulge and disc profiles from *F*444*W* into the UV-plane. This process also involves using a Spergel index ν, empirically determined as a function of the Sérsic index and effective radius (Tan et al. 2024b). We then deblend the ALMA Band-7 flux by fixing the shape parameters (Fig. A1).

APPENDIX C: SED FITTING USING CIGALE

The fluxes measured in the four *JWST* bands and one ALMA band are used in the SED fitting procedure, utilizing the PYTHON based 'Code Investigating GALaxy Emission' (CIGALE; Boquien et al. 2019) tool. CIGALE relies on the energy balance between stellar emission and dust re-emission. Our fitting procedure is similar to that of Kashino et al. (in preparation), but simpler in some aspects to avoid overcomplication due to the limited number of flux measurements. The key details are as follows:

(i) Star-formation history (SFH): given that the galaxies are selected to be star-forming, with clumps particularly active, we adopt a constant SFR with varying duration (age of the main stellar population).

(ii) Single stellar population (SSP): we use the widely adopted Bruzual & Charlot (2003) stellar population synthesis model with the Chabrier (2003) initial mass function, accounting for nebular continuum, and line emission.
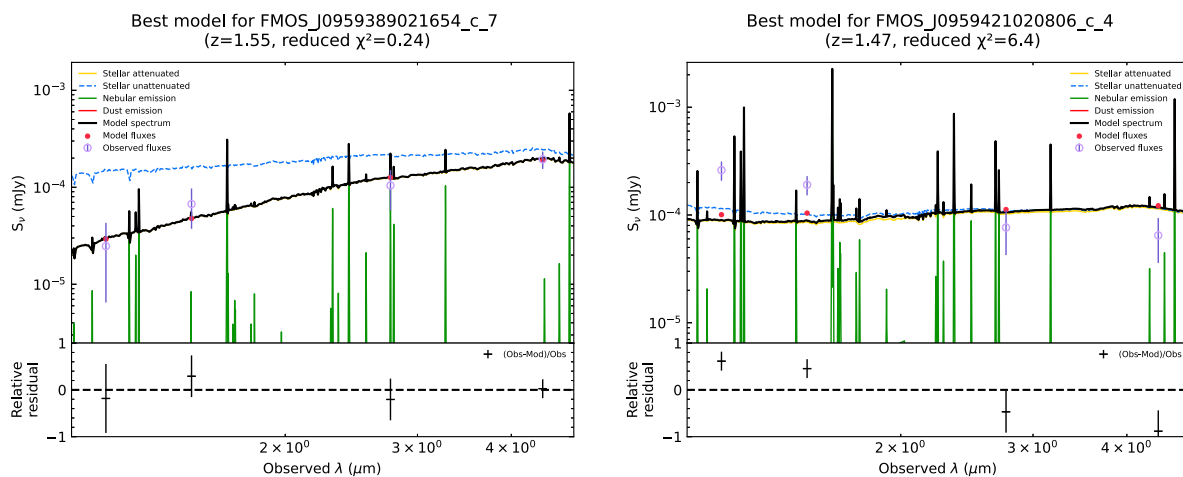
[16]http://www.iram.fr/IRAMFR/GILDAS

Figure C1. SED fit example of a fit for a clump that was included (left) and another that was excluded (right) in our sample.
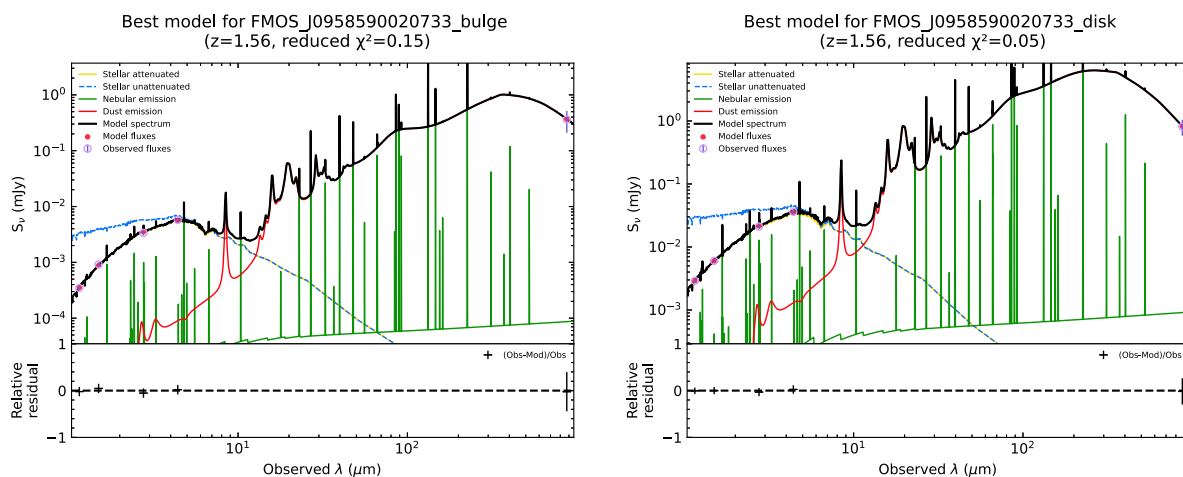

Figure C2. SED fit example with four *JWST* and one ALMA bands of a fit for bulge (left) and disc (right) in source ID 147.
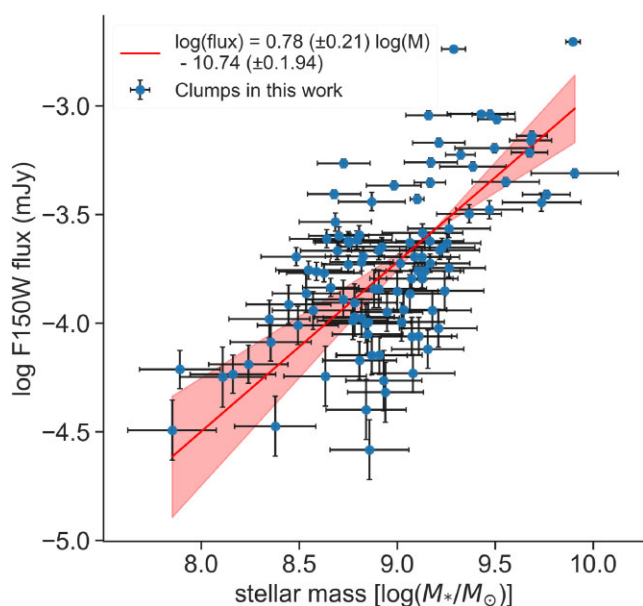

Figure C3. The mass-to-light relation for the clumps in our sample, which relates the *F*150*W* flux to the SED-based stellar mass determination.

(iii) No active galactic nucleus (AGN) template: any AGN hosts, identified using various tracers including X-ray, mid-IR, and broad-line components in Hα, have already been excluded. Additionally, we observe no difference in the measured properties of the bulges and discs when using an AGN template. Thus, we do not use one for our final run.

(iv) Dust: we apply a modified Calzetti law, based on the original model Calzetti et al. (2000) extended between the Lyman break and 150 nm (Leitherer et al. 2002), improving applicability to star-forming galaxies at higher redshifts. We use the Draine & Li (2007) dust emission models to represent the sub-mm flux and the radiation field intensity within the range $U_{min} = 0.1$ to $U_{max} = 10^6$.

(v) Molecular gas mass: the dust masses from the SED fitting are converted to molecular gas mass using the metallicity-dependent gas-to-dust ratio (Magdis et al. 2012), based on the [N II]/Hα ratio (Kashino et al. 2019).

For the bulge and disc measurements, we use the full 5-band photometry (Figs C1 and C2). In the *JWST* bands, the disc flux is the sum[17] of the disc model flux and the flux of clumps within r_{90} of the rest-frame near-IR disc. However, for the clump SED fitting,

[17]With the net error the quadrature sum of individual components.

Table C1. The details of the final 32 galaxies in our sample (Fig. 1). The galaxy stellar masses (Column 5) have been measured using the COSMOS2020 flux catalogue (Weaver et al. 2022) and the same SED fitting recipe used in this work. The last column provides the number of detected clumps in each galaxy that has been included in the final sample. The corresponding number of clumps before rejecting based on χ^2 is also provided within brackets.

| ID	RA (deg)	Dec. (deg)	Spec-z	Stellar mass $\log(M_\star/M_\odot)$	Bulge St. mass $\log(M_\star/M_\odot)$	Bulge SFR $\log(M_\odot\,\mathrm{yr}^{-1})$	Disc St. mass $\log(M_\star/M_\odot)$	Disc SFR $\log(M_\odot\,\mathrm{yr}^{-1})$	Clump count
1987	149.721750	1.965500	1.626438	10.97 ± 0.04	10.25 ± 0.21	2.15 ± 0.22	10.95 ± 0.20	2.15 ± 0.22	0 (4)
147	149.745833	2.125944	1.556338	11.07 ± 0.02	10.07 ± 0.18	2.00 ± 0.20	10.88 ± 0.17	2.00 ± 0.20	3 (5)
1704	149.775542	2.251639	1.673098	10.90 ± 0.04	9.73 ± 0.17	1.83 ± 0.20	10.65 ± 0.16	1.83 ± 0.20	0 (1)
2423	149.825125	1.978889	1.487085	10.91 ± 0.03	10.60 ± 0.17	1.85 ± 0.22	10.45 ± 0.16	1.85 ± 0.22	1 (8)
1943	149.832750	2.024306	1.482637	10.90 ± 0.02	10.06 ± 0.20	1.76 ± 0.17	10.82 ± 0.11	1.76 ± 0.17	1 (3)
1147	149.854708	2.115111	1.481732	11.05 ± 0.08	10.34 ± 0.17	2.01 ± 0.24	10.74 ± 0.20	2.01 ± 0.24	0 (2)
89	149.855750	2.130222	1.478401	11.09 ± 0.03	10.27 ± 0.13	1.74 ± 0.23	10.55 ± 0.18	1.74 ± 0.23	2 (2)
1831	149.877875	2.297639	1.509195	10.96 ± 0.05	10.32 ± 0.15	1.90 ± 0.21	10.71 ± 0.16	1.90 ± 0.21	0 (3)
1766	149.878792	2.499833	1.672921	10.92 ± 0.02	10.36 ± 0.20	2.01 ± 0.17	10.87 ± 0.13	2.01 ± 0.17	3 (3)
682	149.889708	2.358778	1.501451	10.79 ± 0.02	9.96 ± 0.16	1.63 ± 0.20	10.61 ± 0.14	1.63 ± 0.20	2 (6)
326	149.912250	2.281639	1.550443	10.96 ± 0.02	10.40 ± 0.20	1.65 ± 0.16	10.64 ± 0.11	1.65 ± 0.16	7 (8)
2028	149.923208	1.898194	1.552804	11.05 ± 0.02	9.91 ± 0.18	1.89 ± 0.21	10.81 ± 0.16	1.89 ± 0.21	0 (2)
193	149.925333	2.135028	1.470131	10.91 ± 0.05	10.14 ± 0.17	1.85 ± 0.29	10.66 ± 0.18	1.85 ± 0.29	2 (6)
1945	149.938375	1.950056	1.444649	10.88 ± 0.05	9.98 ± 0.23	1.19 ± 0.22	10.15 ± 0.15	1.19 ± 0.22	1 (3)
285	149.972667	2.490139	1.455462	10.92 ± 0.02	9.93 ± 0.18	1.90 ± 0.24	10.65 ± 0.19	1.90 ± 0.24	0 (1)
3074	149.985375	2.561778	1.557741	10.96 ± 0.08	10.23 ± 0.12	1.90 ± 0.22	10.80 ± 0.16	1.90 ± 0.22	1 (2)
2074	149.997875	2.480861	1.462140	11.05 ± 0.02	10.22 ± 0.17	2.07 ± 0.23	10.90 ± 0.17	2.07 ± 0.23	14 (15)
1861	150.001083	2.321444	1.459471	11.00 ± 0.02	10.34 ± 0.17	1.69 ± 0.21	10.59 ± 0.15	1.69 ± 0.21	2 (3)
1749	150.025000	2.355278	1.610989	10.87 ± 0.06	10.30 ± 0.20	1.72 ± 0.23	10.53 ± 0.18	1.72 ± 0.23	2 (3)
281	150.124042	2.447583	1.599120	10.97 ± 0.03	10.61 ± 0.16	1.78 ± 0.22	10.59 ± 0.18	1.78 ± 0.22	3 (3)
81	150.164458	1.936306	1.525303	10.94 ± 0.02	10.09 ± 0.19	1.84 ± 0.21	10.65 ± 0.16	1.84 ± 0.21	7 (8)
2151	150.200875	2.460639	1.582532	10.79 ± 0.04	10.22 ± 0.20	1.70 ± 0.23	10.63 ± 0.16	1.70 ± 0.23	4 (7)
1663	150.220708	2.013139	1.604375	10.86 ± 0.04	10.11 ± 0.17	1.99 ± 0.23	10.81 ± 0.17	1.99 ± 0.23	4 (4)
482	150.258083	2.240167	1.603783	10.89 ± 0.02	10.15 ± 0.13	1.88 ± 0.22	10.72 ± 0.17	1.88 ± 0.22	7 (7)
428	150.292500	2.422167	1.635788	11.05 ± 0.04	10.19 ± 0.15	2.19 ± 0.22	10.96 ± 0.19	2.19 ± 0.22	7 (11)
2905	150.302250	1.931889	1.548028	10.94 ± 0.05	9.89 ± 0.17	1.86 ± 0.19	10.87 ± 0.14	1.86 ± 0.19	4 (7)
1394	150.365458	2.227500	1.699351	11.28 ± 0.05	10.38 ± 0.17	1.99 ± 0.14	11.02 ± 0.11	1.99 ± 0.14	3 (3)
3165	150.394917	2.456361	1.438470	10.74 ± 0.04	10.12 ± 0.17	1.91 ± 0.24	10.65 ± 0.19	1.91 ± 0.24	6 (9)
1334	150.402917	2.408833	1.514096	10.54 ± 0.04	9.93 ± 0.16	1.88 ± 0.20	10.79 ± 0.15	1.88 ± 0.20	3 (7)
852	150.441542	2.129222	1.557442	11.42 ± 0.02	10.44 ± 0.12	2.27 ± 0.23	10.98 ± 0.22	2.27 ± 0.23	6 (10)
4003	150.469292	2.476528	1.579673	10.86 ± 0.10	10.00 ± 0.15	1.69 ± 0.22	10.62 ± 0.16	1.69 ± 0.22	4 (4)
495	150.482708	2.304139	1.485021	10.66 ± 0.02	9.68 ± 0.18	1.90 ± 0.23	10.59 ± 0.18	1.90 ± 0.23	3 (7)
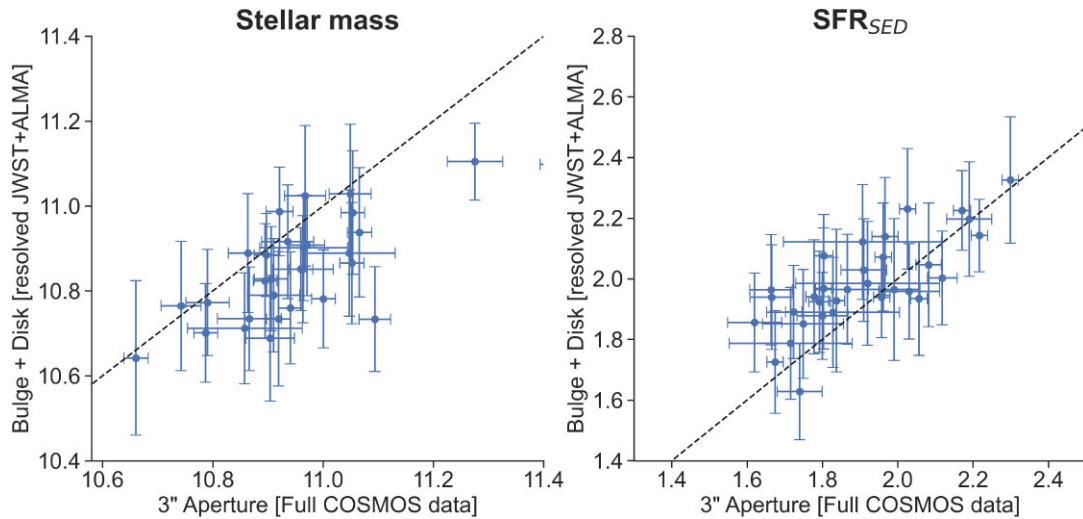
Figure C4. Comparison of the sum of log stellar mass and log SFR measurements for the bulge and the disc, to the results from the 3 arcsec aperture flux measurements of the whole galaxy.

we do not have access to the ALMA Band-7 fluxes and thus perform only a 4-band SED fitting. For both, we use the Hα-determined spectroscopic redshift. We provide the final results in Table C1. We also compare the sum of stellar mass and SFR measurements for the bulge and disc to those from 3 arcsec aperture flux measurements encompassing the complete host (discussed in Section 2.4) in Fig. C4. The respective error bars reflect the uncertainties of the measurements (derived from values at $\Delta\chi^2 = \pm 1$) in the two works.

[1] *Kavli IPMU (WPI), UTIAS, The University of Tokyo, Kashiwa, Chiba 277-8583, Japan*

[2] *Kavli Institute for Astronomy and Astrophysics, Peking University, Beijing 100871, China*

[3] *Centre for Data-Driven Discovery, Kavli IPMU (WPI), UTIAS, The University of Tokyo, Kashiwa, Chiba 277-8583, Japan*

[4] *National Astronomical Observatory of Japan, 2-21-1 Osawa, Mitaka, Tokyo 181-8588, Japan*

[5] *Department of Astronomy, School of Science, The University of Tokyo, 7-3-1 Hongo, Bunkyo, Tokyo 113-0033, Japan*

[6] *Centre for Astrophysical Sciences, Department of Physics & Astronomy, Johns Hopkins University, Baltimore, MD 21218, USA*

[7] *Université Paris-Saclay, Université Paris Cité, CEA, CNRS, AIM, , F-91191 Paris, France*

[8] *Department of Astronomy, School of Physics, Peking University, Beijing 100871, China*

[9] *School of Physics and Technology, Wuhan University, Wuhan 430072, China*

[10] *Aix Marseille Univ., CNRS, CNES, LAM, Marseille, France*

[11] *Caltech/IPAC, MS 314-6, 1200 E. California Blvd. Pasadena, CA 91125, USA*

[12] *NASA Headquarters, 300 Hidden Figures Way, SE, Mary W. Jackson NASA HQ Building, Washington, DC 20546, USA*

[13] *Cosmic Dawn Center (DAWN), Denmark*

[14] *Niels Bohr Institute, University of Copenhagen, Jagtvej 128, DK-2200 Copenhagen N, Denmark*

[15] *School of Physics and Astronomy, University of Southampton, Highfield SO17 1BJ, UK*

[16] *Faculty of Global Interdisciplinary Science and Innovation, Shizuoka University, 836 Ohya, Suruga-ku, Shizuoka 422-8529, Japan*

[17] *Centre for Astrophysics Research, University of Hertfordshire, College Lane, Hatfield AL10 9AB, UK*

[18] *Laboratory for Multiwavelength Astrophysics, School of Physics and Astronomy, Rochester Institute of Technology, 84 Lomb Memorial Drive, Rochester, NY 14623, USA*

[19] *Astrophysics Division, NASA Goddard Space Flight Center, Greenbelt, MD 20771, USA*

[20] *Department of Astronomy, School of Science, The University of Tokyo, 7-3-1 Hongo, Bunkyo, Tokyo 113-0033, Japan*

[21] *DTU-Space, Technical University of Denmark, Elektrovej 327, DK-2800, Kgs. Lyngby, Denmark*

[22] *Purple Mountain Observatory & Key Laboratory for Radio Astronomy, Chinese Academy of Sciences, 10 Yuanhua Road, Nanjing 210023, China*

[23] *Space Telescope Science Institute, 3700 San Martin Dr, Baltimore, MD 21218, USA*

[24] *Department of Astronomy, The University of Texas at Austin, 2515 Speedway Blvd Stop C1400, Austin, TX 78712, USA*

[25] *Department of Astronomy and Astrophysics, University of California, Santa Cruz, 1156 High Street, Santa Cruz, CA 95064, USA*

[26] *Center for Computational Astrophysics, Flatiron Institute, 162 Fifth Avenue, New York, NY 10010, USA*

[27] *Institute of Physics, GalSpec, Ecole Polytechnique Federale de Lausanne, Observatoire de Sauverny, Chemin Pegasi 51, CH-1290 Versoix, Switzerland*

[28] *INAF, Astronomical Observatory of Trieste, Via Tiepolo 11, I-34131 Trieste, Italy*

[29] *Department of Computer Science, Aalto University, P.O. Box 15400, FI-00076 Espoo, Finland*

[30] *Department of Physics, University of Helsinki, P.O. Box 64, FI-00014 Helsinki, Finland*

[31] *SOFIA Science Center, NASA Ames Research Center, Moffett Field CA 94035, USA*

[32] *Department of Physics & Astronomy, University of California Los Angeles, 430 Portola Plaza, Los Angeles, CA 90095, USA*

This paper has been typeset from a TEX/LATEX file prepared by the author.